Inhomogeneous distribution of a rigid fibre undergoing rectilinear flow between parallel walls at high Péclet numbers

JOONTAEK PARK AND JASON E. BUTLER†

Department of Chemical Engineering, University of Florida, Gainesville, FL 32611, USA

We use slender-body theory to simulate a rigid fibre within simple shear flow and parabolic flow at zero Reynolds number and high Péclet numbers (weak Brownian motion). Hydrodynamic interactions of bulk fibres with the bounding walls are included using previously developed methods (Harlen, Sundararajakumar & Koch, *J. Fluid Mech.*, vol. 388, 1999, pp. 355–388; Butler & Shaqfeh, *J. Fluid Mech.*, vol. 468, 2002, pp. 205–237). We also extend a previous analytic theory (Park, Bricker & Butler, *Phys. Rev.* E, vol. 76, 2007, 04081) predicting the centre-of-mass distribution of rigid fibre suspensions undergoing rectilinear flow near a wall to compare the steady and transient distributions. The distributions obtained by the simulation and theory are in good agreement at sufficiently high shear rates, validating approximations made in the theory which predicts a net migration of the rigid fibres away from the walls due to a hydrodynamic lift force. The effect of the inhomogeneous distribution on the effective stress is also investigated.

1. Introduction

The dynamic behaviour and rheological properties of macromolecules or particles suspended in a confined domain can differ from those of unbounded solutions and suspensions due to interactions between the solid boundaries and the bulk particles. These interactions can include those arising from excluded volume constraints and colloidal forces such as electrostatic and van der Waals interactions, and they can also arise from hydrodynamic forces (Agarwal, Dutta & Mashelkar 1994). For example, simulations and theories have clarified that hydrodynamic interaction increases the depletion layer of flexible polymers near bounding walls in shearing flows (Jendrejack *et al.* 2004; Ma & Graham 2005; Hernández-Ortiz, de Pablo & Graham 2006; Usta, Butler & Ladd 2006, 2007; Butler *et al.* 2007).

The origin of the hydrodynamic lift force generating the enhanced depletion of flexible polymers near walls was identified using an elastic dumb-bell model (Ma & Graham 2005). This model indicates that the local shear flow extends the polymer, generating tension in the chain and a resultant perturbation to the flow field around the polymer. When in the vicinity of a bounding wall, the no-slip boundary further modifies the flow perturbation created by the polymer to produce a net velocity away from the wall. This migration, which has been observed qualitatively in experiments by Fang, Hu & Larson (2005), has implications for the design and operation of

† Email address for correspondence: butler@che.ufl.edu

microfluidic devices (Stone, Stroock & Ajdari 2004). As one effect, the lift force hinders adsorption of polyelectrolytes (Hoda & Kumar 2007*a*, *b*, 2008).

A recent simulation and subsequent theory indicate that rigid polymers and Brownian rods within strong shearing flows also migrate away from bounding walls due to hydrodynamic interactions (Saintillan, Shaqfeh & Darve 2006*a*; Park, Bricker & Butler 2007). This result is consistent with experiments on semi-rigid xanthan molecules in pressure-driven flow, which indicate migration away from a wall (Ausserre *et al.* 1991). However, other mechanisms not associated with hydrodynamic interactions with the bounding wall also alter the depletion layer. Simulations and models which consider only steric effects predict that sufficiently strong shear enhances the depletion layer beyond that of the equilibrium distribution (de Pablo, Ottinger & Rabin 1992; Schiek & Shaqfeh 1995). Also, gradients in the diffusivity, caused by the coupling of the anisotropic mobility of the centre of mass of a rod and differences in the shear rate across a channel with pressure-driven flow, shift the distribution closer to the walls (Nitsche & Hinch 1997; Schiek & Shaqfeh 1997).

A previous theoretical investigation (Nitsche & Roy 1996) found that hydrodynamic interactions acting upon a Brownian fibre sheared near a wall have little effect on the depletion layer. That theory considered the limit of weak shear flows only, however. At high rates of shear, the kinetic theory of Park *et al.* (2007) predicts migration arising from three mechanisms, two of them related to hydrodynamic interactions. The third corresponds to the gradient mechanism identified by Nitsche & Hinch (1997) and Schiek & Shaqfeh (1997) that does not depend upon far-field hydrodynamic interactions and moves the rigid fibres closer to the bounding walls on average. Mechanisms which screen hydrodynamic interactions between the fibre and wall would render this term dominant. Screening can occur for fibres with very high aspect ratio and for a separation between bounding walls which is of the length of the fibre or smaller.

The stronger of the two hydrodynamic mechanisms identified by Park *et al.* (2007) is similar to the mechanism described for flexible polymers. The inability of the rigid fibre to deform with the fluid creates an additional flow field which is reflected by a bounding wall to create a transverse motion. This transverse motion can occur towards or away from the bounding wall, depending upon the instantaneous orientation of the rod. The centre of mass of a force and torque-free rod tumbling in a Jeffery orbit due to an imposed shear flow will oscillate transverse to the wall, since the symmetry of the orientation distribution is preserved. This coupling of a shearing flow and a transverse motion has been noted and investigated in past theories and simulations for rod-like particles (Yang & Leal 1984), for prolate spheroids (Hsu & Ganatos 1976; Olla 1999) and even for oblate spheroids (Mody & King 2005). Producing a net migration requires breaking the symmetry of the orientation distribution for the particle tumbling in the shear flow. Kinetic theory predicts that weak Brownian motion alters the rotational dynamics of a rigid fibre in shear flow (Leal & Hinch 1971; Stover, Koch & Cohen 1992; Hijazi & Zoaeter 2002), changing the orientation distribution in a manner that results in a net migration of the fibre away from the wall.

The weaker of the two hydrodynamic mechanisms of migration predicted by the kinetic theory of Park *et al.* (2007) does not have an analogue within the theory for the flexible dumb-bell. This secondary migration arises from a hydrodynamic coupling of the Brownian rotation of the rigid fibre and bounding wall. A particle with an isotropic orientation distribution fluctuates transverse to the wall in response to this interaction, but the shear flow creates a preferential orientation and a consequent lift away from the wall.
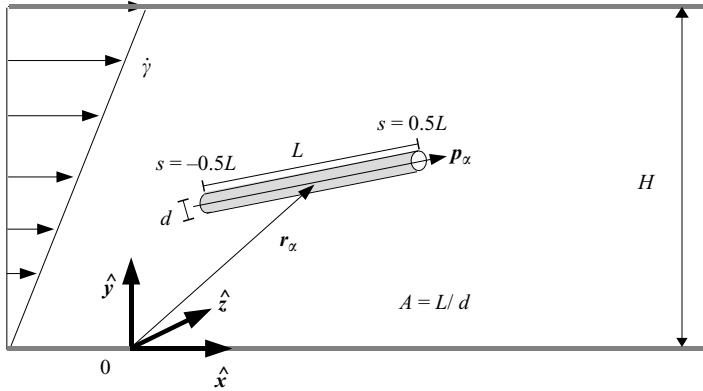
FIGURE 1. A rigid fibre sheared at a rate $\dot{\gamma}$ between two parallel walls separated by a gap of H. The centre-of-mass vector $\boldsymbol{r}_\alpha$ and the orientation vector $\boldsymbol{p}_\alpha$ describe the configuration of the fibre. The aspect ratio A is the ratio of length L to diameter d, and the coordinate s defines positions along the fibre axis ($s = 0$ at the centre of mass). Flow is in the x-direction, and the gradient is in the y-direction.

While the kinetic theory qualitatively predicts the migration observed in the simulations of Saintillan *et al.* (2006*a*), the theory contains multiple approximations. These include solving for the orientation distribution separate from the centre of mass and an evaluation of the hydrodynamic interaction with the wall that lacks rigour in favour of simplicity. Excluded volume interactions of the rigid fibre with the wall were also neglected in the theory. Just as Brownian dynamics simulations have been performed to test kinetic theories for the migration of flexible polymers (Hernández-Ortiz *et al.* 2006; Hoda & Kumar 2007*b*), we test the theory of Park *et al.* (2007) by performing simulations with and without hydrodynamic interactions of a rigid fibre with weak Brownian motion suspended in rectilinear flows between two walls. Comparisons between simulations demonstrate that the depletion layer is affected by hydrodynamics only for very large rates of shear; at moderate rates of shear at which the hydrodynamic mechanism for migration is relatively weak, the thickness of the depletion layer is controlled by excluded volume interactions of the rod with the bounding walls. The distributions obtained by the simulation with hydrodynamic interactions are in good agreement with those predicted by the theory of Park *et al.* (2007) for sufficiently high rates of shear.

The algorithm for performing the simulations is described in §2. We extend the previous theory for predicting the centre-of-mass distribution at steady state for a rigid fibre under shear flow near a wall to a fully analytic expression for shear flow between two bounding walls. The time evolution of the distribution is also calculated from the theory in §3. Results from simulations and the theory are compared for the evolution of the distribution in simple shear flow and the steady distribution in parabolic flows in §4. Additional calculations investigate the effect of the migration on the bulk stress in §5, and conclusions are drawn in §6.

2. Simulation

We simulate a rigid fibre confined between two bounding walls as shown in figure 1. To include hydrodynamic interactions of the bulk particle with bounding walls, we represent each wall as a periodic array of slender bodies and calculate

interactions between all particles using methods based upon previous work (Harlen, Sundararajakumar & Koch 1999; Butler & Shaqfeh 2002). This approach differs from calculation of the Green's function for two planar walls of infinite extent (Liron & Mochon 1976; Staben, Zinchenko & Davis 2003) as done by Saintillan *et al.* (2006*a*). However, representing the walls by closely packed arrays of particles has been used with success in Stokesian dynamics (Nott & Brady 1994; Singh & Nott 2000; Bricker & Butler 2007), and the method can be extended to perform simulations of non-dilute systems, which is a focus of ongoing work. The equations governing the motion of the rigid fibres are derived from slender-body theory as indicated in § 2.1, and additional details of the simulation method are given in § 2.2.

2.1. *Governing equations*

In the absence of inertia and for a Newtonian suspending fluid, the total sum of external forces $\mathscr{F}_\alpha$ and torques $\mathscr{T}_\alpha$ on a fibre α balances the hydrodynamic forces $\mathscr{F}_\alpha^H$ and torques $\mathscr{T}_\alpha^H$,

$$\mathscr{F}_\alpha + \mathscr{F}_\alpha^H = 0 \quad \text{and} \quad \mathscr{T}_\alpha + \mathscr{T}_\alpha^H = 0, \tag{2.1}$$

where the hydrodynamic forces and torques are calculated using slender-body theory at leading order (Batchelor 1970; Cox 1970). Solving for the centre-of-mass velocity for a rigid fibre α gives

$$\dot{\boldsymbol{r}}_\alpha = \frac{1}{L} \int_{-L/2}^{L/2} \boldsymbol{u}_\alpha(s_\alpha) \, \mathrm{d}s_\alpha + \xi^{-1}(\boldsymbol{I} + \boldsymbol{p}_\alpha \boldsymbol{p}_\alpha) \cdot \mathscr{F}_\alpha, \tag{2.2}$$

and the explicit expression for rotational velocity is

$$\dot{\boldsymbol{p}}_\alpha = \frac{12}{L^3}(\boldsymbol{I} - \boldsymbol{p}_\alpha \boldsymbol{p}_\alpha) \cdot \int_{-L/2}^{L/2} \boldsymbol{u}_\alpha(s_\alpha) s_\alpha \, \mathrm{d}s_\alpha + \frac{12\xi^{-1}}{L^3} \mathscr{T}_\alpha \times \boldsymbol{p}_\alpha, \tag{2.3}$$

where $\boldsymbol{I}$ is the identity matrix; $\xi^{-1} = \ln(2A)/4\pi\mu L$; and μ is the fluid viscosity. The total force and torque acting on the fibre are given by moments of the integrated line force density $\boldsymbol{f}_\alpha(s_\alpha)$,

$$\mathscr{F}_\alpha = \int_{-L/2}^{L/2} \boldsymbol{f}_\alpha(s_\alpha) \, \mathrm{d}s_\alpha \quad \text{and} \quad \mathscr{T}_\alpha = \int_{-L/2}^{L/2} s_\alpha \boldsymbol{p}_\alpha \times \boldsymbol{f}_\alpha(s_\alpha) \, \mathrm{d}s_\alpha. \tag{2.4}$$

The fluid velocity $\boldsymbol{u}_\alpha(s_\alpha)$ on a fibre α is the sum of disturbance velocities induced by the force distribution acting on all other fibres β,

$$\boldsymbol{u}_\alpha(s_\alpha) = \sum_{\beta=1}^{N} \int_{-L/2}^{L/2} \boldsymbol{G}(s_\alpha, s_\beta) \cdot \boldsymbol{f}_\beta(s_\beta) \, \mathrm{d}s_\beta, \tag{2.5}$$

where $\boldsymbol{G}(s_\alpha, s_\beta)$ is the Green's function for periodic point forces on the fluid and N is the total number of fibres in the system. The coordinate s_α is the point of evaluation on fibre α of the velocity disturbance induced by the line force density at point s_β on fibre β. In this simulation, the Green's function given by Beenakker (1986), which is the Ewald-summed expression of the Green's function by Rotne & Prager (1969) in a periodic system, is used. For the special case of $\alpha = \beta$, the Green's function for free space must be subtracted from $\boldsymbol{G}(s_\alpha, s_\beta)$. In the event that $\alpha = \beta$ and $s_\alpha = s_\beta$, the limiting form given by Beenakker (1986) is used.

For dynamic simulations of suspensions of hydrodynamically interacting rigid fibres, the solution of Hasimoto (1959) for the periodic Oseen–Burger tensor has
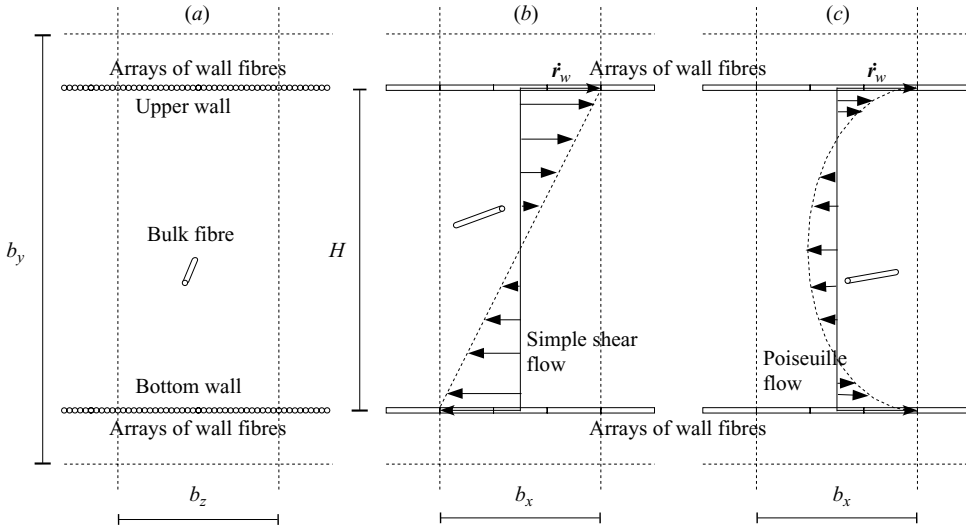
FIGURE 2. Arrays of closely packed fibres form the walls in a periodic boundary system of dimensions b_x, b_y and b_z. (*a*) A view from the vorticity-gradient zy-plane; (*b*) view of simple shear flow; and (*c*) parabolic flow from the flow-gradient xy-plane.

been widely used (Harlen *et al.* 1999; Butler & Shaqfeh 2002; Saintillan, Shaqfeh & Darve 2006*b*). However, this results in a mobility tensor which sometimes lacks the property of being positive definite when a pair of fibres are in close proximity. The solution of Beenakker (1986) ensures a positive definite matrix for any configuration of the interacting particles regardless of separation distance, so it has been applied to these simulations due to the presence of closely packed arrays of fibres which form the walls. Tornberg & Gustavsson (2006) also used Beenakker's (1986) solution in the simulation of sedimenting rigid fibres. Comparing the velocity disturbance generated by a force on a fibre by integrating Oseen–Burger tensor and Beenakker's (1986) solution along the length of the rod demonstrates that the error is negligible at a distance of three times the fibre diameter. For the specific case of a force acting perpendicular to a rod centred at the origin, the velocity disturbances in the perpendicular direction agree within 5 % at a distance of two diameters for a point located on the plane lying perpendicular to the rod and centred on the rod.

To facilitate numerical calculation, the force distribution $f_\beta(s_\beta)$ is linearized (Harlen *et al.* 1999; Butler & Shaqfeh 2002),

$$f_\beta(s_\beta) = \frac{1}{L}\mathscr{F}_\beta + \frac{12s_\beta}{L^3}[\mathscr{T}_\beta \times p_\beta + S_\beta p_\beta], \qquad (2.6)$$

where the stresslet coefficient is given by

$$S_\beta = -\frac{\xi}{2L}\int_{-L/2}^{L/2} s_\beta p_\beta \cdot u_\beta(s_\beta)\,\mathrm{d}s_\beta. \qquad (2.7)$$

The relation between the stresslet coefficient and the particle stress is discussed in §5. Subsequent substitutions of (2.5) with (2.6) into (2.2) and (2.3) gives a linear set of equations relating forces and motions of the fibres.

We identify two types of particles in this simulation: wall fibres and a bulk fibre. Closely packed arrays of the wall fibres form the two planar boundaries as shown in figure 2. The bulk fibre is contained in the space between the upper wall and the

bottom wall in a periodic box, but not in the space between the wall and its adjacent image wall.

For the wall fibres, the velocities

$$\boldsymbol{v}_W = (\dot{\boldsymbol{r}}_W \quad \dot{\boldsymbol{p}}_W) \tag{2.8}$$

are specified, and we solve for the forces

$$\boldsymbol{F}_W = (\boldsymbol{\mathscr{F}}_W \quad \boldsymbol{\mathscr{T}}_W \times \boldsymbol{p}_W). \tag{2.9}$$

This resistance problem is simultaneously solved with the equations for the stresslet coefficients on the wall fibres S_W and bulk fibre S_B,

$$\begin{pmatrix} \boldsymbol{F}_W \\ \boldsymbol{\mathscr{S}}_W \\ \boldsymbol{\mathscr{S}}_B \end{pmatrix} = \begin{pmatrix} \mathscr{M}_{WW}^{VF} & \mathscr{M}_{WW}^{VS} & \mathscr{M}_{WB}^{VS} \\ \mathscr{M}_{WW}^{EF} & \mathscr{M}_{WW}^{ES} & \mathscr{M}_{WB}^{ES} \\ \mathscr{M}_{BW}^{EF} & \mathscr{M}_{BW}^{ES} & \mathscr{M}_{BB}^{ES} \end{pmatrix}^{-1} \cdot \left[\begin{pmatrix} \boldsymbol{v}_W \\ \boldsymbol{0}_W \\ \boldsymbol{0}_B \end{pmatrix} - \begin{pmatrix} \mathscr{M}_{WB}^{VF} \\ \mathscr{M}_{WB}^{EF} \\ \mathscr{M}_{BB}^{EF} \end{pmatrix} \cdot \boldsymbol{F}_B \right], \tag{2.10}$$

where the forces on the bulk fibre

$$\boldsymbol{F}_B = (\boldsymbol{\mathscr{F}}_B \quad \boldsymbol{\mathscr{T}}_B \times \boldsymbol{p}_B) \tag{2.11}$$

affect the forces on the wall fibres necessary to maintain their steady motion. The tensors $\mathscr{M}$ in (2.10) relate the motion and forces. The superscripts represent the type of motion and force which are related by the matrix, and the subscripts designate the fibres which correspond to related motion and force. For example, $\mathscr{M}_{WB}^{VF}$ represents the tensor which relates the force and torque on the bulk fibre to the motions of the wall fibre. Each component of a matrix $\mathscr{M}$ is a double integral of the Green's function in (2.5) over two fibres (Butler & Shaqfeh 2002). Stresslet coefficients on each fibre are designated by the vector $\mathscr{S}$. Since the fluid motion is generated by moving the wall particles, the rates of strain corresponding to an imposed flow have been set to zero in (2.10); this does not mean that the fibres experience no straining flow but that the straining flow is generated by the relative motion of the particles only. Using the results from (2.10), the motion of the bulk fibre confined between the two parallel walls is given by

$$\boldsymbol{v}_B = \begin{pmatrix} \dot{\boldsymbol{r}}_B \\ \dot{\boldsymbol{p}}_B \end{pmatrix} = \mathscr{P} \cdot \begin{pmatrix} \boldsymbol{v}_W \\ \boldsymbol{0}_W \\ \boldsymbol{0}_B \end{pmatrix} + \mathscr{Q} \cdot \boldsymbol{F}_B, \tag{2.12}$$

where $\mathscr{P}$ represents the response of the motion of the bulk fibre to the shear flow,

$$\mathscr{P} = (\mathscr{M}_{BW}^{VF} \quad \mathscr{M}_{BW}^{VS} \quad \mathscr{M}_{BB}^{VS}) \cdot \begin{pmatrix} \mathscr{M}_{WW}^{VF} & \mathscr{M}_{WW}^{VS} & \mathscr{M}_{WB}^{VS} \\ \mathscr{M}_{WW}^{EF} & \mathscr{M}_{WW}^{ES} & \mathscr{M}_{WB}^{ES} \\ \mathscr{M}_{BW}^{EF} & \mathscr{M}_{BW}^{ES} & \mathscr{M}_{BB}^{ES} \end{pmatrix}^{-1}, \tag{2.13}$$

and $\mathscr{Q}$ is the mobility of the bulk rod,

$$\mathscr{Q} = -\mathscr{P} \cdot \begin{pmatrix} \mathscr{M}_{WB}^{VF} \\ \mathscr{M}_{WB}^{EF} \\ \mathscr{M}_{BB}^{EF} \end{pmatrix} + \mathscr{M}_{BB}^{VF}. \tag{2.14}$$

The Brownian forces and torques acting on the bulk fibre can be obtained from the inverse of the mobility matrix $\mathscr{Q}$ by satisfying the fluctuation dissipation theorem,

$$\boldsymbol{F}_B = \sqrt{\frac{2k_B T}{\Delta t}} \mathscr{B} \cdot \mathscr{W}, \tag{2.15}$$

where

$$\mathscr{B} \cdot \mathscr{B}^T = \mathscr{Q}^{-1}; \tag{2.16}$$

the thermal energy is $k_B T$; and the vector $\mathscr{W}$ contains random numbers generated from a uniform distribution of zero mean and a variance of one. Cholesky decomposition is used to evaluate $\mathscr{B}$ as explained by Butler & Shaqfeh (2005) and Saintillan, Shaqfeh & Darve (2006c).

2.2. *Simulation details*

This simulation method can be used to study fibres flowing at any value of the Péclet number, but simulations are performed at relatively high values at which the phenomena of interest are predicted to strongly impact the distribution of the fibres. We use the given algorithm to simulate the dynamics of a rigid fibre having an aspect ratio of $A = 10$ for all cases. Likewise, the simulations calculate the specific case of a wall separation of $H = 6L$, and one (bulk) fibre is simulated at a time, with averages performed over multiple runs and blocks of time to generate distributions as stated in §4. The bounding walls are constructed of $2b_x b_z / Ld$ fibres of aspect ratio 10. The mobility matrices, consisting of dual integrals over the particle lengths, are generated using a five-point and six-point Gaussian quadrature for the cases of simple shear and parabolic flow, respectively.

To generate simple shear flow, the wall particles are assigned a velocity v_x in the x-direction but with opposite signs for particles in the 'top' and 'bottom' walls; all other velocities are set to zero. For a simple shear flow, the velocity $v_x = \pm H\dot{\gamma}/2$ generates a shear flow of $\dot{\gamma}$. Both walls translate in the positive x-direction at the same velocity of $H\bar{\gamma}/3$ to produce a parabolic flow with a local shear rate of

$$\dot{\gamma}(y) = 2\bar{\gamma}\left(\frac{2y}{H} - 1\right), \tag{2.17}$$

where $\bar{\gamma}$ is the mean shear rate. In both cases the result corresponds closely to the desired, theoretical profiles, and there is no net flow through the yz-plane, since the periodic sums were constructed to ensure zero net flow through any plane. The flow profiles, shown in figure 3, were generated using (2.5) with the linearized force distribution in (2.6) and in the absence of a bulk particle. In addition, we confirmed that fluid does not flow perpendicular to the walls.

Lubrication interactions dominate when the bulk particle approaches within one fibre diameter of the wall. This short-range interaction is added directly to the resistance matrix, using methods identical to those of Butler & Shaqfeh (2002). The interaction itself depends upon the relative orientation of the rod with respect to the wall and is evaluated using the method of Claeys & Brady (1989). The lubrication interaction is supplemented by a short-range repulsive force,

$$\boldsymbol{f}_R = \pm 0.01 \xi \bar{\gamma} \frac{\exp(-10h/L)}{1 - \exp(-10h/L)} \hat{\boldsymbol{y}}, \tag{2.18}$$

where h is the closest distance between the fibre and the bounding wall; the force acts to push the fibre away from the wall; and $\hat{\boldsymbol{y}}$ is the unit vector in the y-direction.
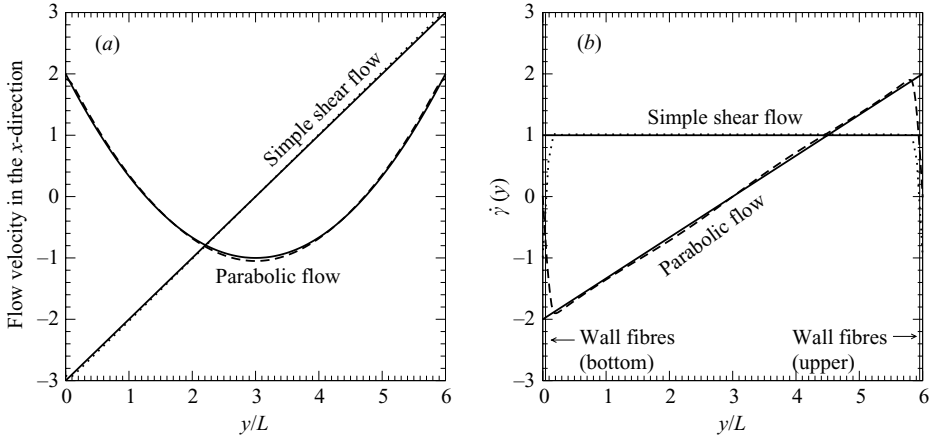
FIGURE 3. Simulation results (broken lines) of (*a*) the velocity profile in the *x*-direction (units of $L\bar{\gamma}$) and (*b*) the local shear rate $\dot{\gamma}(y)$ (units of $\bar{\gamma}$) of the shear flow generated by moving walls as functions of distance from the bottom wall, y/L. Fibres have an aspect ratio of $A = 10$, and the walls are separated by a gap of $H = 6L$ in a periodic box of dimensions $b_x : b_y : b_z = 3L : 8L : 3L$ for simple shear flow and $b_x : b_y : b_z = 3L : 12L : 3L$ for parabolic flow. Theoretical values are plotted as solid lines.

When evaluating the separation between the bulk fibre and the wall, the end tip of the fibre is regarded as a hard sphere having the same diameter as the fibre. This repulsive force is included with the forces and torques acting on the bulk fibre and the wall fibres. Simulation results confirm that the particle does not cross the wall. We also tested other algorithms for maintaining the excluded volume (de Pablo *et al.* 1992; Hijazi & Khater 2001), but the differences in distributions were small.

To distinguish the effects of the hydrodynamic and excluded volume interactions on the depletion layer, simulations are also performed in the absence of hydrodynamic interactions with the walls. These simulations are performed using (2.2) and (2.3) with the velocity $\boldsymbol{u}_B(s_B)$ replaced by the theoretical expression for simple shear flow or parabolic flow as appropriate. The Brownian forces and torques are calculated using the fluctuation dissipation theorem but with the mobility of a single rod suspended in an infinite fluid. The same repulsive force given in (2.18) prevents the fibre from crossing the wall.

Equation (2.12) is integrated using the modified midpoint method; this method integrates the trajectories of the stochastic motion accurately at first order without requiring an explicit evaluation of the divergence of the mobility (Fixman 1978; Grassia, Hinch & Nitsche 1995; Morse 2004). The time step for integrating positions is set to $0.001\bar{\gamma}^{-1}$. Note that many of the submatrices in (2.13) need to be calculated only once. The self-mobilities and any lubrication interactions for the bulk fibre are updated at each time step, but the long-range hydrodynamic interactions between the bulk particle and wall particles are updated less frequently at intervals of $0.05\bar{\gamma}^{-1}$. Tests on this integration scheme demonstrated convergence of the results while greatly decreasing the computational expense of the calculations.

3. Extended theory for centre-of-mass distribution

We extend the previous theory (Park *et al.* 2007) predicting the centre-of-mass distribution of rigid fibres under shear flows near a single wall to a fully analytic

expression for the steady distribution between two bounding walls in §3.1. Additionally, a solution for the time evolution of the distribution is presented in §3.2.

As in the original theory of Park *et al.* (2007), multiple approximations are made. To enable solution of the conservation equation for distribution function, the orientation distribution is solved independent of the centre-of-mass distribution, and restrictions on the allowable orientation due to excluded volume for rigid fibres near the walls are ignored. Also, development of a manageable expression for the migration velocity requires an approximate evaluation of the Green's function. Each simplification is discussed in turn.

3.1. *Steady-state distribution*

The conservation equation for the probability distribution function $\Psi(\boldsymbol{r}_B, \boldsymbol{p}_B, t)$ is given by

$$\frac{\partial \Psi}{\partial t} = -\frac{\partial}{\partial \boldsymbol{r}_B} \cdot (\dot{\boldsymbol{r}}_B \Psi) - (\boldsymbol{I} - \boldsymbol{p}_B \boldsymbol{p}_B) : \frac{\partial}{\partial \boldsymbol{p}_B} (\dot{\boldsymbol{p}}_B \Psi). \tag{3.1}$$

For the rigid fibre, Ψ is factorized into a product of a centre of mass n and orientation ψ distribution,

$$\Psi(\boldsymbol{r}_B, \boldsymbol{p}_B, t) = n(\boldsymbol{r}_B, t)\, \psi(\boldsymbol{r}_B, \boldsymbol{p}_B, t), \tag{3.2}$$

where $n = \int \Psi \, \mathrm{d}\boldsymbol{p}_B$. Integrating (3.1) over the orientation distribution and solving for the steady state gives

$$0 = -\frac{\partial}{\partial \boldsymbol{r}_B} \cdot (n \langle \dot{\boldsymbol{r}}_B \rangle), \tag{3.3}$$

where the angle brackets $\langle\,\rangle$ indicate an ensemble average over orientation, $\int \cdots \psi \, \mathrm{d}\boldsymbol{p}_B$.

Determining n from (3.3) necessitates development of an explicit expression for the transverse velocity. This expression was derived from slender-body theory by Park *et al.* (2007),

$$\dot{r}_y = \dot{\gamma}\lambda(r_y) p_x p_y \left(1 - 3p_y^2\right) + \xi^{-1}(\hat{\boldsymbol{y}} + p_y \boldsymbol{p}_B) \cdot \mathscr{F}_B$$
$$+ \frac{24}{L^2}\xi^{-1}\lambda(r_y)(3p_y\hat{\boldsymbol{y}} - \boldsymbol{p}_B) \cdot (\mathscr{T}_B \times \boldsymbol{p}_B), \tag{3.4}$$

where

$$\lambda(r_y) = \frac{L^3}{128 \ln(2A)} \left[\frac{1}{r_y^2} - \frac{1}{(r_y - H)^2}\right]; \tag{3.5}$$

$\dot{r}_y$ is the y-component of $\boldsymbol{r}_B$; and p_x and p_y are the x- and y-component of $\boldsymbol{p}_B$ respectively. The unit vector in the y-direction is denoted as $\hat{\boldsymbol{y}}$. This expression for $\dot{r}_y$ was derived from (2.2) using (2.4)–(2.7). The evaluation of the Green's function in (2.5) requires two approximations to arrive at the result given in (3.4). First, the proper, two-wall Green's function of Liron & Mochon (1976) is too complicated to manipulate analytically and is consequently approximated by a linear superposition of the Green's function for a single wall (Blake 1971). Furthermore, the Green's function is linearized under the assumption that the rod is far from each of the bounding walls.

The first term on the right-hand side of (3.4) corresponds to the shear flow contribution to the transverse motion and matches the result given by Saintillan *et al.* (2006a). The Brownian force on the centre of mass results in a fluctuation in the y-position, but less obvious is the prediction of a transverse velocity due to the Brownian torque which appears as the third contribution in (3.4).

The Brownian force and torque in (3.4) are expressed in terms of the distribution function,

$$\mathscr{F}_B = -k_B T \frac{\partial \ln \Psi}{\partial \mathbf{r}_B} \quad \text{and} \quad \mathscr{T}_B \times \mathbf{p}_B = -k_B T \left(\mathbf{I} - \mathbf{p}_B \mathbf{p}_B \right) \cdot \frac{\partial \ln \Psi}{\partial \mathbf{p}_B}. \tag{3.6}$$

After performing an average of $\dot{r}_y$ over the orientation distribution function, the average transverse velocity of a rigid fibre $\langle \dot{r}_y \rangle$ is multiplied by n to give the particle flux as a function of position,

$$n\langle \dot{r}_y \rangle = n\dot{\gamma}\lambda(r_y)\left[\langle p_x p_y \rangle - 3\langle p_x p_y{}^3 \rangle\right] - \frac{k_B T}{\xi}\left[\left(1 + \langle p_y^2 \rangle\right)\frac{\partial n}{\partial r_y} + n\frac{\partial \langle p_y^2 \rangle}{\partial y}\right]$$

$$- 72n\frac{k_B T}{\xi L^2}\lambda(r_y)\left(3\langle p_y^2 \rangle - 1\right). \tag{3.7}$$

Integrating (3.3), using (3.7) and the condition of no particle flux through the bounding walls ($n\langle \dot{r}_y \rangle = 0$), gives an equation for the steady-state distribution,

$$\frac{\partial \ln n}{\partial r_y} = \frac{\lambda(r_y)\langle K \rangle + \langle \Gamma \rangle}{\langle D^* \rangle}. \tag{3.8}$$

Here, $\langle K \rangle$ contains the contributions to migration due to hydrodynamic interaction with the bounding walls,

$$\langle K \rangle = \left[\langle p_x p_y \rangle - 3\langle p_x p_y{}^3 \rangle + \frac{72}{Pe}\left(1 - 3\langle p_y^2 \rangle\right)\right]\dot{\gamma}, \tag{3.9}$$

where the Péclet number Pe is defined as

$$Pe = \frac{\dot{\gamma}L^2}{D_T} = \frac{\dot{\gamma}L^2\xi}{k_B T} \tag{3.10}$$

and D_T is the translational diffusivity of a slender body in an infinite fluid (Doi & Edwards 1986). The quantity $\langle p_x p_y \rangle - 3\langle p_x p_y{}^3 \rangle$ is the contribution to transverse motion from the imposed shear flow due to inclusion of the stresslet coefficient, and $72(1 - 3\langle p_y^2 \rangle)/Pe$ is the contribution arising from the Brownian torque. At $Pe = 0$ or $Pe = \infty$, where the orientation distribution is symmetric, $\langle K \rangle$ becomes 0. However, we will show that the asymmetric orientation distribution at high values of Pe results in a positive value for $\langle K \rangle$ and a migration away from the bounding walls. The term $\langle D^* \rangle$ represents the diffusion component acting perpendicular to the wall,

$$\langle D^* \rangle = \frac{1 + \langle p_y^2 \rangle}{Pe}L^2\dot{\gamma}, \tag{3.11}$$

and $\langle \Gamma \rangle$ corresponds to the contribution arising from the anisotropic diffusivity of a rigid polymer,

$$\langle \Gamma \rangle = -\frac{\partial}{\partial y}\left[\frac{\langle p_y^2 \rangle}{Pe}\right]L^2\dot{\gamma}, \tag{3.12}$$

that was previously identified by Nitsche & Hinch (1997) and Schiek & Shaqfeh (1997).

Park *et al.* (2007) calculated the ensemble averages of orientation moments needed within (3.8) by numerically solving the governing equation for the orientation
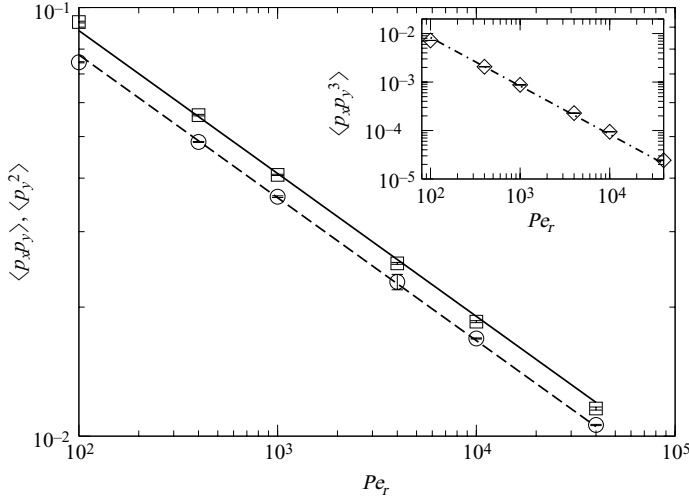
FIGURE 4. Ensemble averages of orientation moments of a slender body as functions of Pe_r: ($\square$), $\langle p_y^2 \rangle \approx 0.41 Pe_r^{-1/3}$; ($\bigcirc$), $\langle p_x p_y \rangle \approx 0.36 Pe_r^{-1/3}$; and ($\diamond$), $\langle p_x p_y^3 \rangle \approx 0.83 Pe_r^{-1}$. Symbols denote the numerical solutions, and lines are the scalings with coefficients determined by the best fit to the numerical data.

distribution. The equation is derived by applying (3.2) to (3.1) at steady state,

$$n\left(\boldsymbol{I} - \boldsymbol{p}_B \boldsymbol{p}_B\right) : \frac{\partial}{\partial \boldsymbol{p}_B}\left(\dot{\boldsymbol{p}}_B \psi\right) = -\frac{\partial}{\partial \boldsymbol{r}_B} \cdot \left(n \dot{\boldsymbol{r}}_B \psi\right). \tag{3.13}$$

Approximating $\dot{\boldsymbol{r}}_B \psi$ by $\langle \dot{\boldsymbol{r}}_B \rangle$ in (3.13) and applying (3.3) gives

$$\left(\boldsymbol{I} - \boldsymbol{p}_B \boldsymbol{p}_B\right) : \frac{\partial}{\partial \boldsymbol{p}_B}\left(\dot{\boldsymbol{p}}_B \psi\right) = 0. \tag{3.14}$$

Equation (3.14) assumes that the orientation distribution equilibrates much faster than particles migrate or diffuse across streamlines.

A further assumption that rotation is not influenced by hydrodynamic or steric interactions with the bounding walls gives a position-independent expression for the rotational velocity,

$$\dot{\boldsymbol{p}}_B = \dot{\gamma} p_y(\hat{\boldsymbol{x}} - p_x \boldsymbol{p}_B) - \frac{12}{\xi L^2}\left(\boldsymbol{I} - \boldsymbol{p}_B \boldsymbol{p}_B\right) \cdot \frac{\partial \ln \psi}{\partial \boldsymbol{p}_B}, \tag{3.15}$$

where $\hat{\boldsymbol{x}}$ is a unit vector in x-direction. Replacing $\dot{\boldsymbol{p}}_B$ in (3.14) with (3.15) and simplifying gives

$$\left(\boldsymbol{I} - \boldsymbol{p}_B \boldsymbol{p}_B\right) : \frac{\partial^2 \psi}{\partial \boldsymbol{p}_B \partial \boldsymbol{p}_B} = Pe_r\left(\boldsymbol{I} - \boldsymbol{p}_B \boldsymbol{p}_B\right) : \frac{\partial}{\partial \boldsymbol{p}_B} \cdot \left[p_y\left(\hat{\boldsymbol{x}} - p_x \boldsymbol{p}_B\right) \psi\right], \tag{3.16}$$

where Pe_r is the rotary Péclet number defined as

$$Pe_r = \frac{\dot{\gamma}}{D_R} = \frac{\dot{\gamma}\xi L^2}{12 k_B T} = \frac{Pe}{12} \tag{3.17}$$

and D_R is the rotational diffusivity of a slender body in an unbounded fluid (Doi & Edwards 1986).

Numerical solution of (3.16) at high values of Pe_r gives the orientation moments shown in figure 4. Our numerical solution was obtained from a series of Brownian
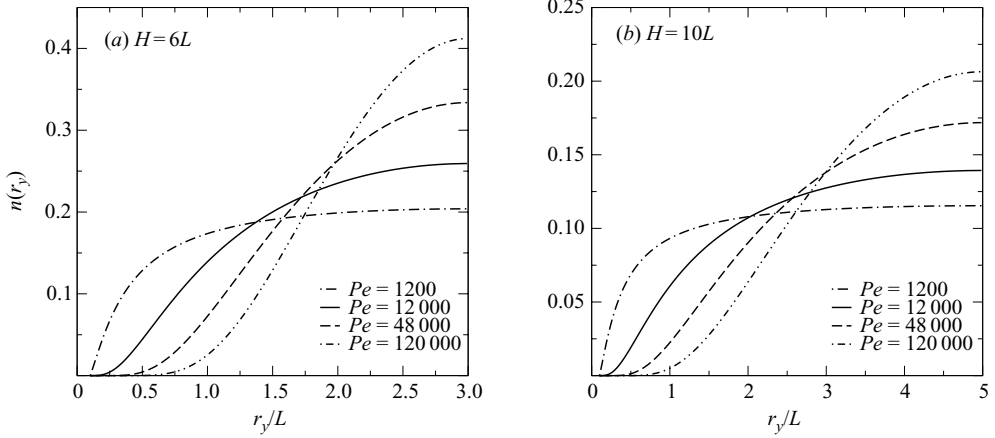
FIGURE 5. The steady-state centre-of-mass distributions $n(r_y)$ of a rigid fibre predicted by (3.18) as functions of distance from a wall, r_y/L, with $A = 10$ and (a) $H = 6L$ and (b) $H = 10L$ in simple shear flow.

dynamics simulations for a single fibre in an infinite fluid using the algorithm of Cobb & Butler (2005). The scalings with Pe_r of the orientation moments shown in figure 4 agree closely with those derived for slender bodies in shear at high Pe_r (Leal & Hinch 1971; Hinch & Leal 1972; Brenner 1974). Following the approach of Chen & Koch (1996), the coefficients of the scalings are determined from a best fit to the numerical data over the range of $10^2 \leqslant Pe_r \leqslant 4 \times 10^4$. Although we fit a wider range of Pe_r than that fitted by (Chen & Koch 1996) ($10^2 \leqslant Pe_r \leqslant 10^3$), the reported coefficients for the orientation moments $\langle p_x p_y \rangle$ and $\langle p_x^2 p_y^2 \rangle$ match. Agreement was also found between the numerical data produced by the Brownian dynamics algorithm and calculations for $Pe_r \geqslant 10^3$ by Chen & Jiang (1999) and for $0 < Pe_r \leqslant 10^3$ by Asokan, Ramamohan & Kumaran (2002). The relationships determined from the data in figure 4 are used within (3.8), which is then integrated for the case of simple shear with $\langle \Gamma \rangle = 0$ to give

$$n(r_y) = \mathscr{C} \exp\left[\frac{HL^3}{128 \ln(2A) r_y (r_y - H)} \frac{\langle K \rangle}{\langle D^* \rangle}\right], \tag{3.18}$$

where the normalization constant $\mathscr{C}$ is determined so that $\int n \, dr_y = 1$. The values of $\langle D^* \rangle$ and $\langle K \rangle$ are given by

$$\langle D^* \rangle = [Pe^{-1} + 0.94 Pe^{-4/3}] L^2 \dot{\gamma} \tag{3.19}$$

and

$$\langle K \rangle = [0.82 Pe^{-1/3} + 42 Pe^{-1} - 200 Pe^{-4/3}] \dot{\gamma}, \tag{3.20}$$

where the correlations for the orientation moments have been used. Note that all Pe_r have been converted to Pe using (3.17). Equation (3.18) is a fully analytic expression for simple shear between two bounding walls which corresponds to a numerical result given by Park et al. (2007) for a single bounding wall with simple shear.

Setting $A = 10$, the steady-state centre-of-mass distributions between two parallel walls under simple shear flows for various $Pe \geqslant 1.2 \times 10^3$ are calculated using (3.18); the results are displayed in figure 5 for $H = 6L$ and $10L$. As mentioned after (3.9), the symmetry of the orientation distribution is broken, and $\langle K \rangle$ is positive. As Pe
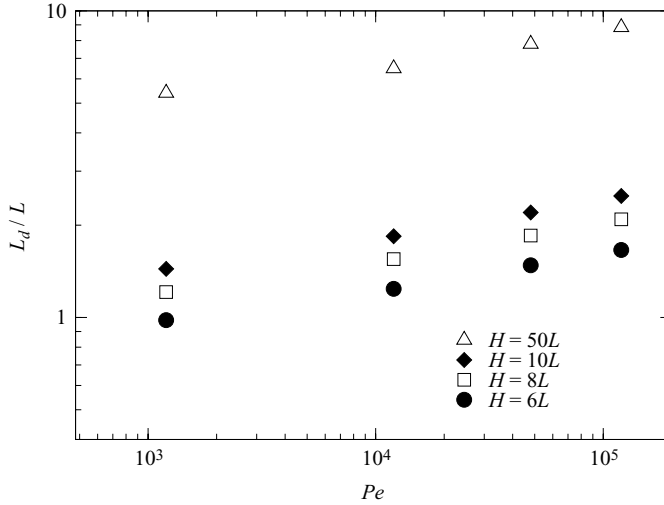
FIGURE 6. The steady-state depletion-layer thickness L_d/L of a rigid fibre of aspect ratio $A = 10$ predicted by (3.18) as a function of Pe and H in simple shear flow.

increases, the ratio between the migration and the diffusion, $\langle K \rangle / \langle D^* \rangle$, increases; therefore the rigid fibres distribute more strongly towards the centre of the channel. Comparing the distributions in the wider and narrower channel demonstrates that reducing the level of confinement increases the depletion layer. The depletion layer L_d, defined as the point r_y at which n returns to the bulk value, is calculated from (3.18) and plotted in figure 6 for $A = 10$ and different values of Pe and H. The increased hydrodynamic lift associated with increasing the shear rate, to give a higher value of Pe, generates a larger depletion layer. Furthermore, increasing the channel width while holding Pe constant extends the depletion layer further into the channel. Though not plotted, the depletion layer also depends upon the aspect ratio, since the hydrodynamic lift varies as $1/\ln(2A)$ as seen in (3.4). Consequently, increasing the aspect ratio reduces the depletion, since the hydrodynamic interaction between the wall and fibre become screened.

3.2. Time evolution of distribution

The evolution of the centre-of-mass distribution under simple shear flow is obtained from the time-dependent version of (3.3),

$$\frac{\partial n}{\partial t} = -\frac{\partial}{\partial y}(n\langle \dot{r}_y \rangle). \tag{3.21}$$

Using the formula for average fibre flux derived in (3.7) with the orientation moments obtained in figure 4 under the same assumptions made in the previous section, the governing equation becomes

$$\frac{\partial n}{\partial t} = \langle D^* \rangle \frac{\partial^2 n}{\partial y^2} - \langle K \rangle \frac{\partial}{\partial y}[n\lambda(r_y)]. \tag{3.22}$$

This equation is similar to the evolution equation for the centre-of-mass distribution of a flexible polymer as derived by Ma & Graham (2005). For the flexible polymers, $\langle K \rangle$ is related to the coupling of the restoring spring force and shear flow, which induces a flow disturbance and migration away from the wall, while $\langle K \rangle$ in (3.22)
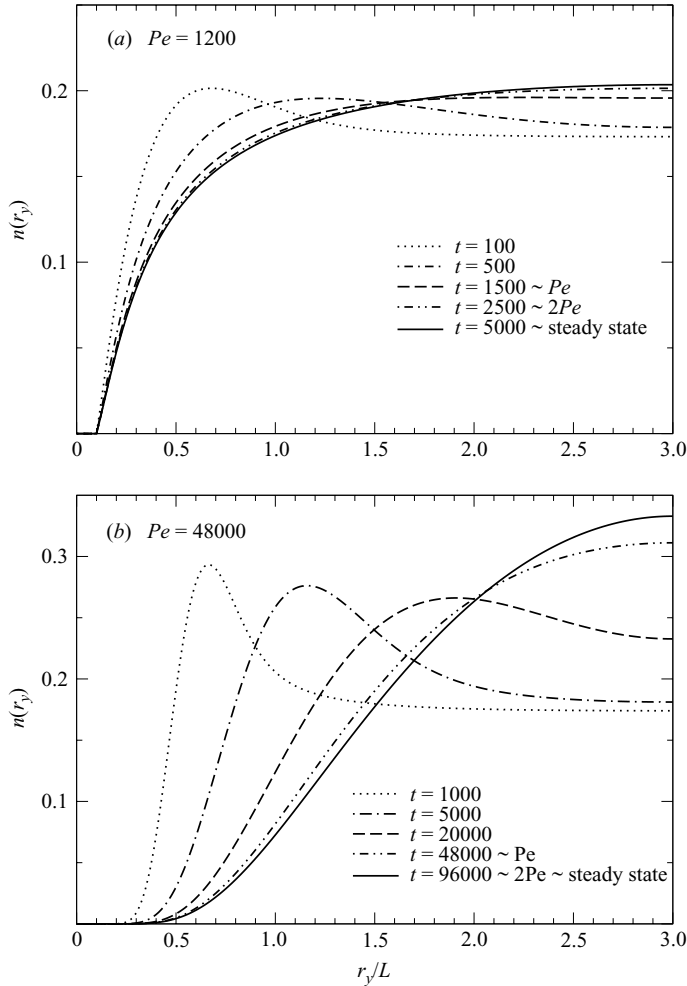
FIGURE 7. The transient centre-of-mass distributions of a rigid fibre predicted by (3.22) as functions of distance from a wall, r_y/L, with $A = 10$ and $H = 6L$ in simple shear flows of (a) $Pe = 1.2 \times 10^3$ and (b) $Pe = 4.8 \times 10^4$. The units of time t are $\dot{\gamma}^{-1}$.

relates the coupling of the stresslet coefficient, or inability of the fibre to stretch, and Brownian torque with the shear flow.

Equation (3.22) is solved numerically using the Crank–Nicolson scheme with an initially uniform distribution and the boundary condition of no flux of the centre of mass through a wall. The time step $\Delta t = 0.01\dot{\gamma}^{-1}$ and position step $\Delta y = 0.001L$ give convergent numerical results that are shown in figure 7. At short times, a peak appears near each wall. As time proceeds, the peak gradually moves towards the centre and becomes more blunt. At a time comparable to $Pe\dot{\gamma}^{-1}$, the peaks from the two walls merge, and the distribution is fully developed at a time of about $2Pe\dot{\gamma}^{-1}$. Since the migration velocity due to hydrodynamic interactions is much larger near a wall, the rigid fibres accumulate near the wall faster than diffusion can smooth the profile. At higher Pe, migration is much stronger than diffusion; therefore, the peak is much sharper near the wall for $Pe = 4.8 \times 10^4$ than $Pe = 1.2 \times 10^3$. As time passes, the migration and diffusion of fibres balances, and the distribution reaches steady state.

An upper bound on the time t_S to achieve steady state can be estimated as the time for a rigid fibre to diffuse from the wall to the centre of the channel,

$$t_S = \frac{H^2/4}{2\langle D^* \rangle} \sim O\left(\frac{Pe\,H^2}{8L^2\dot\gamma}\right), \tag{3.23}$$

where $\langle D^* \rangle$ is approximated using the leading order of Pe^{-1} in expression (3.19). This estimate for t_S at $H = 6L$ is about twice as large as indicated by the results in figure 7. Ma & Graham (2005) argued that a flexible polymer needs to diffuse only a distance equivalent to the depletion width, whereas we find that the distributions at $t = 2Pe\dot\gamma^{-1}$ are virtually identical to the steady distributions.

4. Results

Comparisons between the results of the simulation and the theory are presented in the following sections. We demonstrate that the calculations are in good agreement for the prediction of the configuration-dependent lift velocity (§4.1), the steady and unsteady distribution in simple shear flow (§4.2) and the steady distribution in parabolic flow (§4.3).

4.1. *Transverse velocity due to shear flow*

The primary mechanism for migration of a rigid fibre in a strong shear flow is the transverse velocity, coupled with a preferential orientation, resulting from hydrodynamic interactions with the wall. An explicit expression for the transverse velocity due to shear as a function of configuration is embodied in the first term of (3.4),

$$\dot r_y = \dot\gamma\,\lambda(r_y)p_x p_y \left(1 - 3p_y^2\right). \tag{4.1}$$

The response of a fibre to the shear flow can be determined from the simulation using (2.12) by setting $\boldsymbol{F}_B$ to 0 and extracting the y-component of the velocity,

$$\dot r_y = \hat{\boldsymbol{y}} \cdot \boldsymbol{v}_B = \hat{\boldsymbol{y}} \cdot \mathscr{P} \cdot \begin{pmatrix} \boldsymbol{v}_W \\ \boldsymbol{0}_W \\ \boldsymbol{0}_B \end{pmatrix}. \tag{4.2}$$

Comparisons between the theoretical analysis (4.1) and computational result (4.2) appear in figures 8 and 9.

Figure 8 compares the dependence of the transverse velocity on angle ϕ (the angle between the x-axis and projection of $\boldsymbol{p}_B$ onto the xy-plane as illustrated) for a fibre fixed at a distance $1L$ from the wall. The results match qualitatively, with the largest quantitative discrepancies occurring at orientations corresponding to the secondary maximum of $\dot r_y$. The quantitative differences between the calculations of transverse velocity also depend upon the position of the fibre and size of the periodic box as shown in figure 9.

Causes of the quantitative discrepancies clearly include the approximations made for the evaluation of the Green's function used in the analytic expression. The theory overestimates the transverse velocity near the centre due to superimposition of the effect of the two bounding walls. The theory was derived by linearizing the Green's function, assuming that the fibre is far from the wall in comparison to its length; the increasing discrepancy with the simulated results as the fibre approaches the wall can be attributed to the breakdown of this assumption. Though the solution given by the numerical calculation avoids key problems associated with the theoretical evaluation,
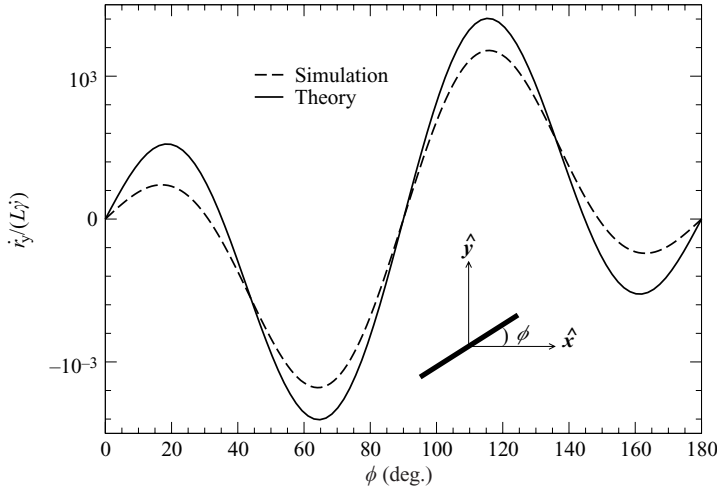
FIGURE 8. Transverse velocity $\dot{r}_y$ due to shear flow as a function of angle ϕ with $p_z = 0$, $r_y = 1.0L$ and $H = 6L$. Simulation conditions are the same as those in figure 3(b) with simple shear flow. The inset illustrates a rigid fibre with an angle ϕ and $p_z = 0$.
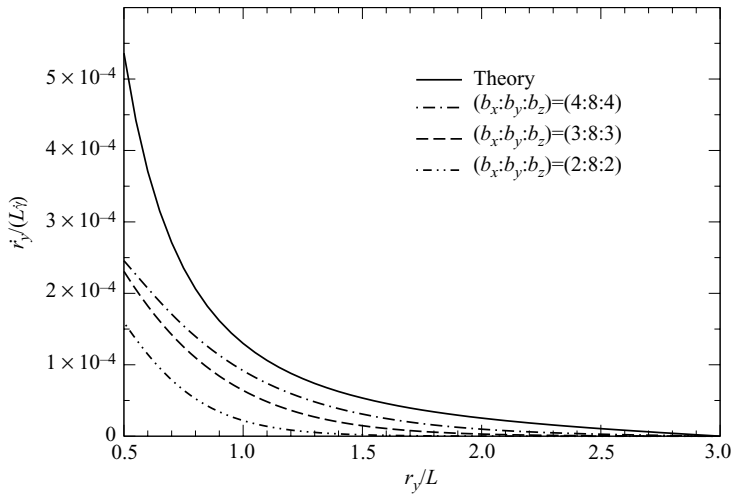

FIGURE 9. Transverse velocity $\dot{r}_y$ due to shear contribution as a function of distance from a wall, r_y/L, for a fixed angle ($\phi = 3°$ and $p_z = 0$) under a constant shear rate $\dot{\gamma}$. Results are shown for the theory and three simulations with different periodic dimensions.

the 'bumpy' wall formed by the array of fibres and the use of the periodic Green's function represent sources of error. With regard to the periodicity, changing the box height b_y or ratio between H and b_y (distance between one wall and neighbouring image wall) makes little difference, but changing the area of the xz-plane alters the results as shown in figure 9. Due to periodicity, the transverse velocity predicted by the simulation is lower than expected for a single rod suspended between two plates of infinite extent.

We also performed tests on the components of $\dot{r}_y$ arising from forces and torques given in (3.4). Comparisons of these terms with the responses from simulations also

demonstrate a qualitative match and quantitative differences similar to those observed for the shear contribution.

4.2. *Distributions in simple shear flow*

Simulations of the rigid fibre in simple shear flow were performed with a total of 32 different runs for each value of Pe. Initial orientations and positions were chosen randomly, and positions were sampled during the simulations to produce the centre-of-mass distribution. The results are compared with the transient and steady-state distributions predicted in §3.2.

Figure 10 shows the time evolution of centre-of-mass distribution in simple shear flow for $Pe = 1.2 \times 10^3$. The distributions exhibit a maximum near the wall at short times (figure 10*a*), with a larger maximum produced by the simulation than the theory. While the theory predicts attainment of a steady-state distribution around $t = 2Pe\dot{\gamma}^{-1}$, the distribution averaged over times of $t = 2500 \sim 5000\dot{\gamma}^{-1}$ (figure 10*b*) still shows significant variations around the predicted distribution which is at steady state. The simulated distribution conforms closely to the theoretical distribution at steady state (figure 10*c*) when averaged over long times.

The good agreement shown in figure 10 between the results of the theory and simulation with hydrodynamic interaction is fortuitous. Simulations with and without hydrodynamic interactions with the walls at $Pe = 1.2 \times 10^3$ produce a nearly identical distribution as shown in figure 10(*c*). The similarity establishes that excluded volume, which the theory does not consider, is controlling the distribution; the flow strength at $Pe = 1.2 \times 10^3$ is too low to generate clear evidence of the hydrodynamic lift. The results in figure 10(*c*) are also consistent with previous investigations (de Pablo *et al.* 1992; Schiek & Shaqfeh 1995) of the changes in the depletion layer due to shear and excluded volume. We note that the distribution becomes uniform at a value of about $0.6L \sim 0.7L$, rather than $0.5L$, since the end of the rod is a hemisphere that extends an additional distance of $0.1L$ beyond $0.5L$ and since the surface of the wall is corrugated.

Simulated distributions with hydrodynamic interactions at $Pe = 1.2 \times 10^4$ are shown in figure 11. The transient maximum near the wall appears early in the simulation results (figure 11*a*) and agrees with the theoretical prediction within the averaging errors. The intermediate distribution (figure 11*b*) fluctuates around the corresponding theoretical distribution, and the distribution for $t > 17\,000\dot{\gamma}^{-1}$ (figure 11*c*) closely corresponds to the theoretical steady state.

The steady distribution from simulations without hydrodynamic interaction at $Pe = 1.2 \times 10^4$ is plotted in figure 11(*c*). As compared to the corresponding result at $Pe = 1.2 \times 10^3$ in figure 10(*c*), the depletion layer increases because of the higher rate of shear but still does not extend beyond $r_y \approx 0.65L$, where the distribution becomes uniform. Comparing the distributions from simulations at $Pe = 1.2 \times 10^4$ with and without hydrodynamic interaction demonstrates that the hydrodynamic interactions strongly influence the distribution in a manner consistent with the theoretical prediction.

Figure 12 shows distributions from simulation with hydrodynamic interaction at $Pe = 4.8 \times 10^4$. Although the averaging errors are large at short times, the transient off-centre maximum is detectable in the mean values. The simulation was terminated at $t \sim Pe\dot{\gamma}^{-1}$ owing to the computational burden, though the distribution is continuing to develop. The distribution from simulation without hydrodynamic interaction in figure 12(*c*) demonstrates a clear difference as compared to the one with hydrodynamic interaction, indicating again the role played by the hydrodynamic lift force.
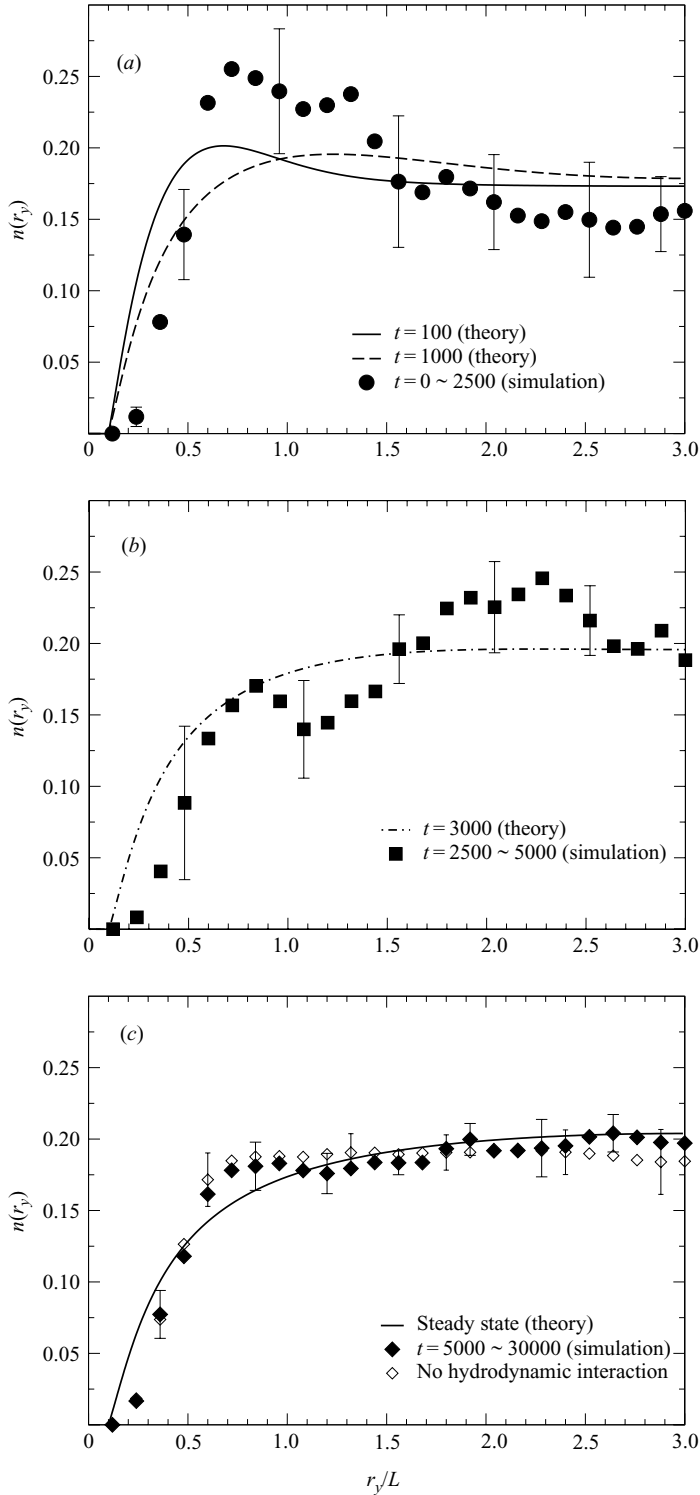
FIGURE 10. The simulation results (symbols) and theoretical solutions (lines) for the transient centre-of-mass distributions of a rigid fibre as functions of distance from a wall, r_y/L, with $A = 10$ and $H = 6L$ in simple shear flows of $Pe = 1.2 \times 10^3$. Simulation results are averaged over the time ranges (units of $\dot{\gamma}^{-1}$) as indicated in each sub-part.
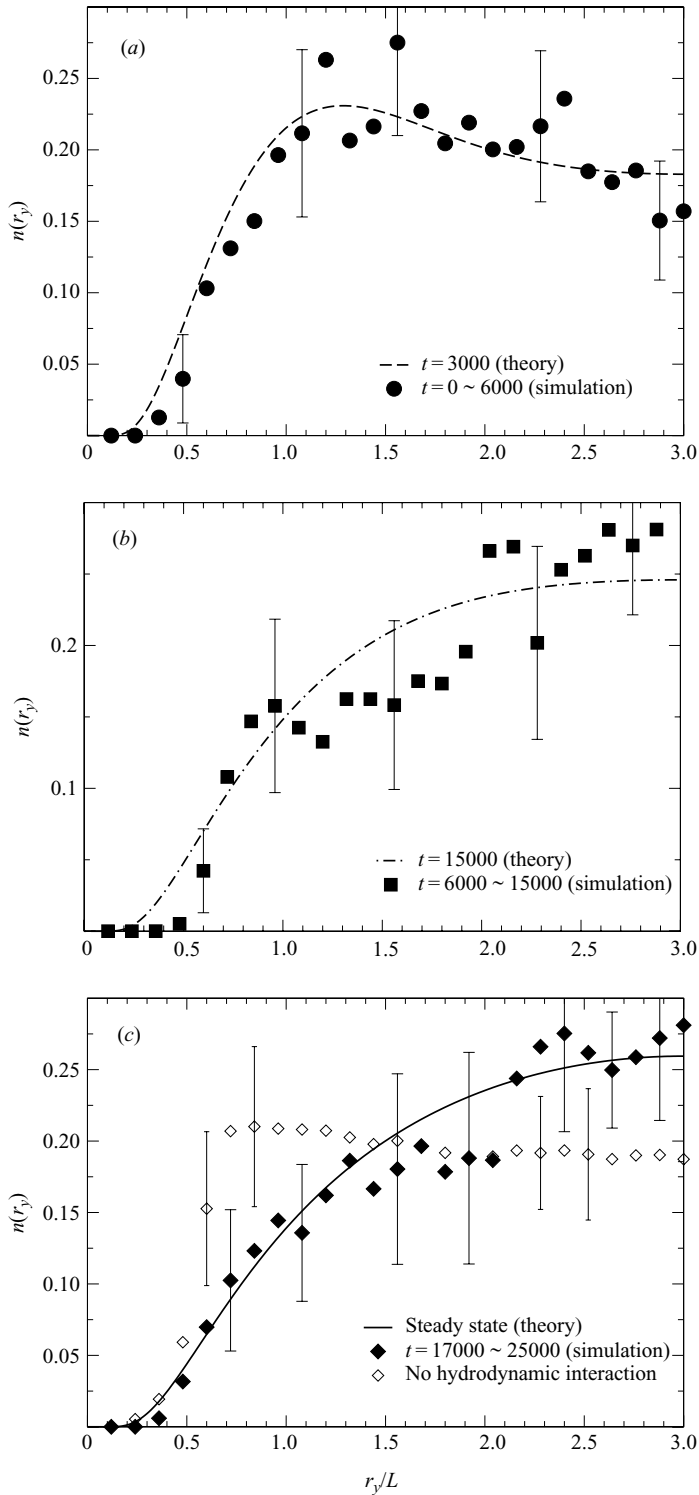
FIGURE 11. The simulation results (symbols) and theoretical solutions (lines) for the transient centre-of-mass distributions of a rigid fibre as functions of distance from a wall, r_y/L, with $A = 10$ and $H = 6L$ in simple shear flows of $Pe = 1.2 \times 10^4$. Simulation results are averaged over the time ranges (units of $\dot{\gamma}^{-1}$) as indicated in each sub-part.
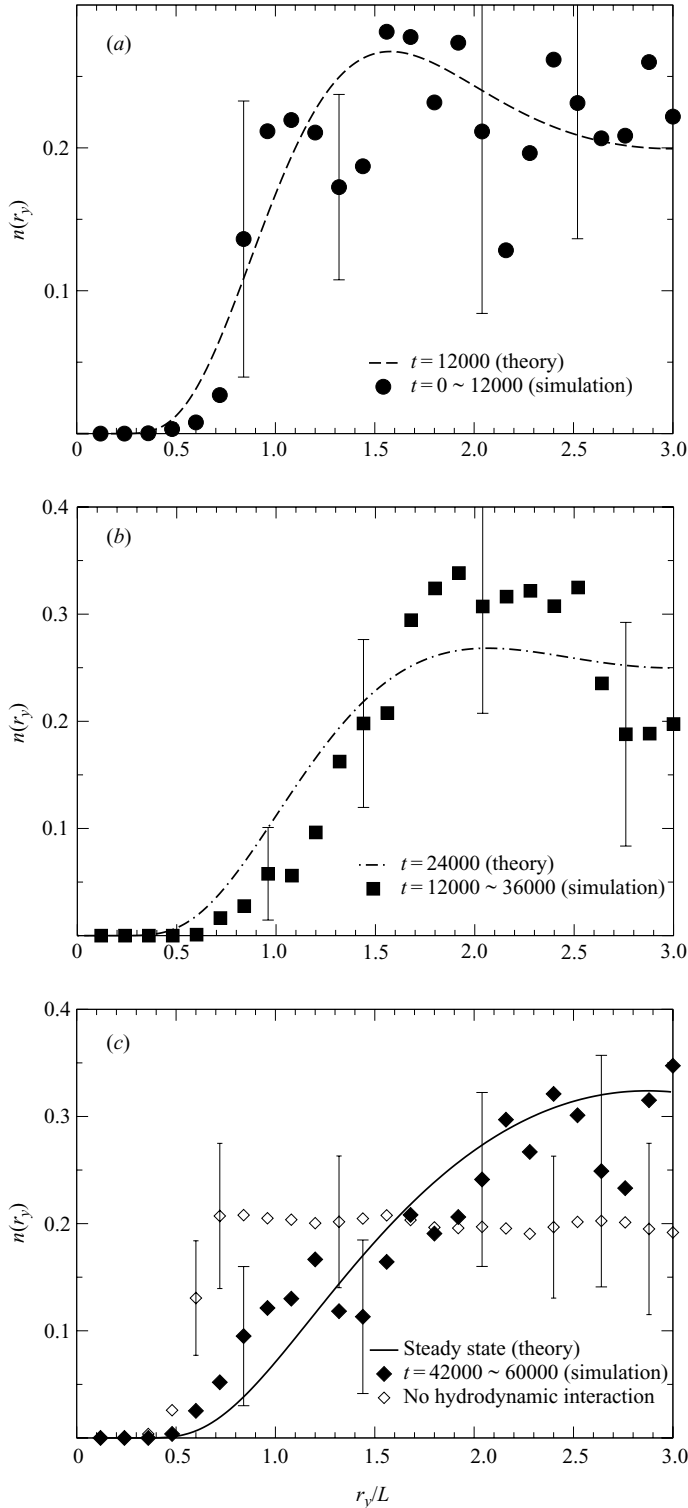
FIGURE 12. The simulation results (symbols) and theoretical solutions (lines) for the transient centre-of-mass distributions of a rigid fibre as functions of distance from a wall, r_y/L, with $A = 10$ and $H = 6L$ in simple shear flows of $Pe = 4.8 \times 10^4$. Simulation results are averaged over the time ranges (units of $\dot{\gamma}^{-1}$) as indicated in each sub-part.
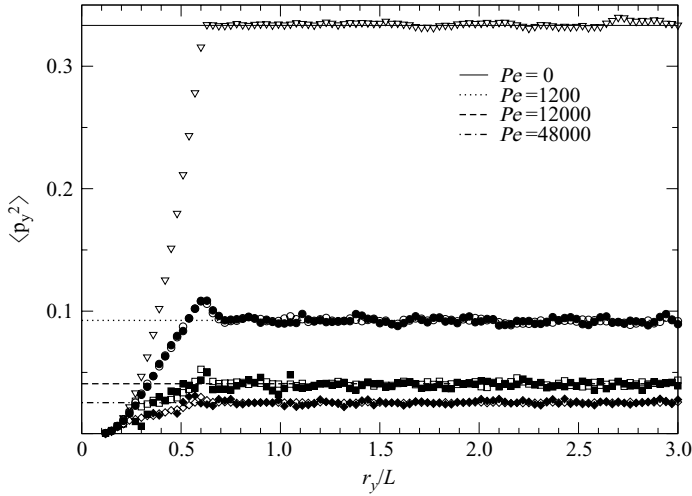
FIGURE 13. The simulation results with (filled symbols) and without (open symbols) hydrodynamic interactions for the orientation moment $\langle p_y^2 \rangle$ of a rigid fibre as functions of distance from a wall, r_y/L, with $A = 10$ and $H = 6L$. The expected values of $\langle p_y^2 \rangle$ for unbounded flow are plotted as lines.

Figure 13 shows the orientation moment $\langle p_y^2 \rangle$ calculated from the simulations as a function of position and Pe; the orientation moments for unbounded flow, which are used to make the theoretical prediction, are also shown. The values of $\langle p_y^2 \rangle$ from simulations with and without hydrodynamic interaction have no discernible differences regardless of distance from the wall, confirming the assumption made within the theory that hydrodynamic interaction with the walls does not affect the orientation distribution. The wall affects the orientation through excluded volume interactions for $r_y < 0.7L$, resulting in substantial differences with the orientation distribution assumed within the theoretical calculations.

The overshoot of $\langle p_y^2 \rangle$ around $0.65L$ for finite shear rates is an interesting feature observable in figure 13. The action of the short-range repulsive force with the wall on the end of a rod rotating in the shear flow creates a 'pole-vault-type' of motion that displaces the rods, oriented nearly perpendicular to the wall, outwards to give the enhanced probability of $\langle p_y^2 \rangle$ in the range of $r_y = 0.6L \sim 0.7L$. Though the effect is likely caused by the repulsive force, attempts to eliminate the overshoot by altering the strength and range of the repulsive force were unsuccessful. We note that 'pole-vault' motions have been observed by others in simulations (Stover & Cohen 1990; Mody & King 2005) in the absence of Brownian motion and even in experiments (Holm & Söderberg 2007).

In the vicinity of a wall ($r_y \lesssim 0.7L$), the steric effects control the orientation distribution, and ignoring the excluded volume within the theory is clearly in error. However, the neglect of excluded volume has a limited effect on the theoretical prediction of the centre-of-mass distribution for values of Pe above 1.2×10^3. The primary reason is that few fibres remain within a distance of $0.7L$ of the bounding walls for the higher shear rates due to the hydrodynamic migration away from the wall.

The qualitative features of the centre-of-mass distributions predicted by the theory appear in the simulations for $Pe = 1.2 \times 10^4$ and 4.8×10^4: the transient maximum near

the walls forms at short times, then moves towards the centre while broadening and disappears at $t \sim Pe\dot{\gamma}^{-1}$. Quantitative comparisons of transient profiles are hindered by the larger errors in some of the results, but the overall good agreement verifies that the errors associated with assumptions made in the theory do not have severe adverse affects on the prediction so long as the depletion layer extends beyond the range at which the rotation of the rod is hindered by the wall.

4.3. *Steady-state distribution in parabolic flow*

Simulations were performed under parabolic flow to produce a long-time distribution for three values of $\overline{Pe} = \bar{\gamma}L^2/D_T$ as shown in figure 14. The number of runs, initial configuration and sampling method match those of simulations for simple shear flow presented in § 4.2. The distributions are compared with the steady distributions obtained by numerically integrating (3.8). The orientation moments used within (3.8) depend upon position according to the local shear rate as given by solution to (3.16); alterations in the orientation due to hydrodynamic interactions or excluded volume are ignored as was done for the calculations in simple shear.

At $\overline{Pe} = 1.2 \times 10^3$, the theory and simulation with hydrodynamic interaction generate a similar concentration profile, although the results from simulations are noisy due to averaging errors. However, the simulation in the absence of hydrodynamic interaction gives nearly the same result. As in the case of simple shear at a similar Pe, the hydrodynamic lift has little effect upon the near-wall distribution for this and lower values of Pe. Clear differences are observed between simulations with and without hydrodynamic interaction for $\overline{Pe} = 1.2 \times 10^4$ and 4.8×10^4, indicating that the excluded volume interactions are not causing the strong depletion near the wall. The good agreement between the results from the simulation with hydrodynamic interaction and the theory, which does not consider excluded volume, provides further evidence that the balance between Brownian diffusion and the hydrodynamic lift primarily controls the distribution for these higher values of Pe.

The simulations of a Brownian rigid fibre in parabolic flow by Saintillan *et al.* (2006*a*) were performed at $\overline{Pe} = 50$ and 300. The authors' suggestion that the results were due to a hydrodynamic lift, similar to that identified for flexible polymers, motivated the kinetic theory of Park *et al.* (2007). The current results imply that the depletion observed by Saintillan *et al.* (2006*a*) was mostly due to steric effects. However, the simulations of Saintillan *et al.* (2006*a*) were also performed in a wider channel of $H = 8L$ and without periodic boundaries, where the hydrodynamic lift would be expected to be stronger.

The results of the simulations without hydrodynamic interactions and theory exhibit an off-centre maximum due to the gradient in diffusivity induced by the variation in shear rate across the channel (Nitsche & Hinch 1997; Schiek & Shaqfeh 1997). Evidence of the off-centre maximum is difficult to detect in the simulations with interactions due to large averaging errors, though figure 14(*b*) seems to demonstrate a reduction in the distribution near the centreline of the channel. The lack of a clear off-centre maximum may be due in part to the orientation distribution. Figure 15 shows that the gradient in $\langle p_y^2 \rangle$, which causes the migration towards the wall through the term $\langle \Gamma \rangle$ in (3.8), is smaller than assumed in the theoretical description. Note that figure 15 also shows an overshoot in $\langle p_y^2 \rangle$ at $r_y = 0.6L \sim 0.7L$, similar to the results for the case of simple shear flow.
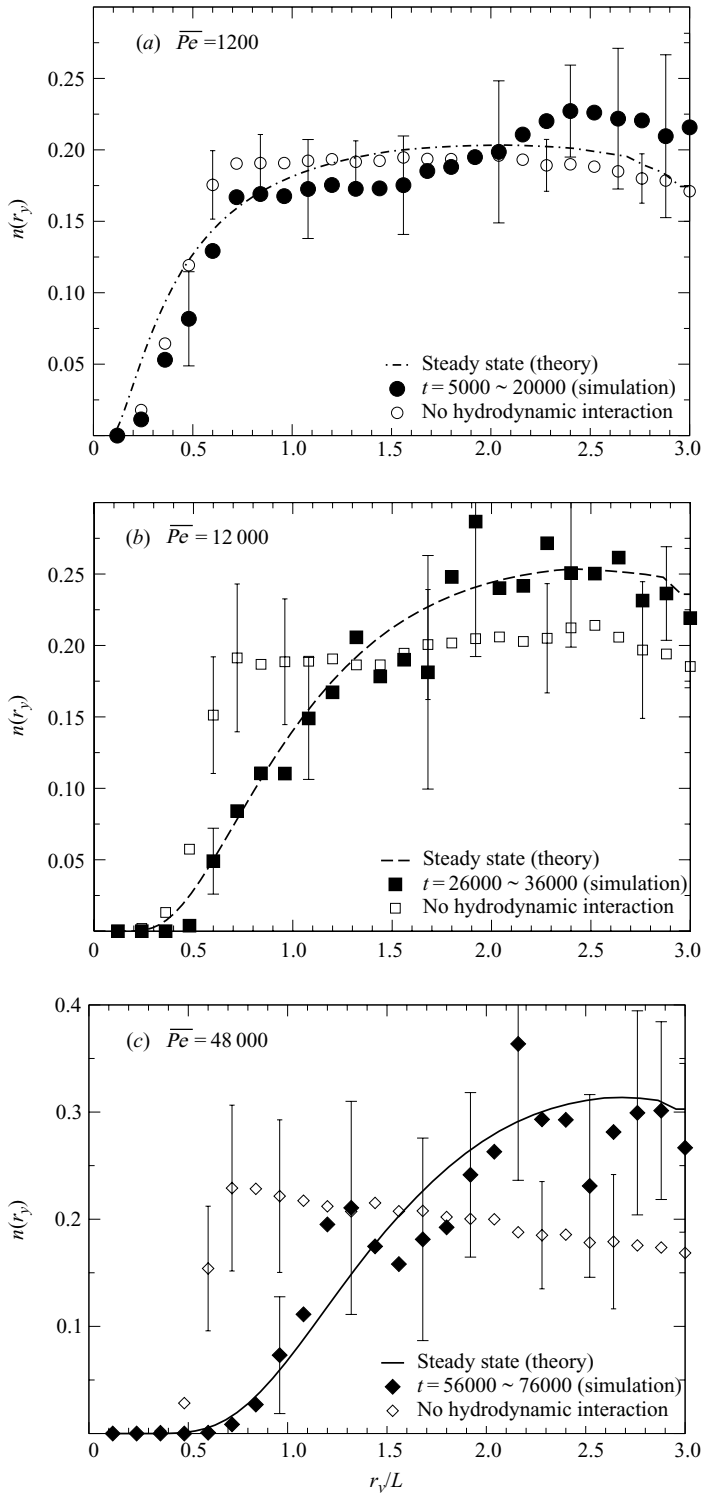
FIGURE 14. The simulation results (symbols) and theoretical solutions (lines) for the centre-of-mass distributions of a rigid fibre as functions of distance from a wall, r_y/L, with $A = 10$ and $H = 6L$ in parabolic flows of (a) $\overline{Pe} = 1.2 \times 10^3$, (b) $\overline{Pe} = 1.2 \times 10^4$ and (c) $\overline{Pe} = 4.8 \times 10^4$. The time (units of $\overline{\dot{\gamma}}^{-1}$) ranges at which the simulation data were taken are indicated in each sub-part.
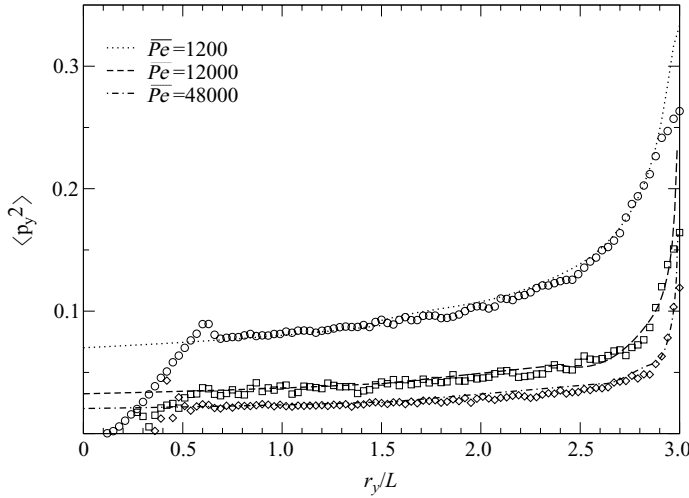
FIGURE 15. The simulation results with hydrodynamic interactions (symbols) for $\langle p_y^2 \rangle$ of a rigid fibre as functions of distance from a wall, r_y/L, with $A = 10$ and $H = 6L$ in parabolic flows of $\overline{Pe} = 1.2 \times 10^3$ ($\bigcirc$), $\overline{Pe} = 1.2 \times 10^4$ ($\square$) and $\overline{Pe} = 4.8 \times 10^4$ ($\diamond$). The corresponding values for unbounded flow that account for the position-dependent rate of shear are plotted as dashed lines.

5. Stress calculation

The effective stress of a Newtonian suspension of viscosity μ, sheared at a rate $\dot{\gamma}$, is

$$\overline{\boldsymbol{\sigma}} = -P\boldsymbol{I} + 2\mu\boldsymbol{E} + \overline{\boldsymbol{\sigma}}^P, \tag{5.1}$$

where P is the fluid pressure; $\boldsymbol{E}$ is the rate of strain tensor which satisfies $\dot{\gamma} = (1/2)(\boldsymbol{E} : \boldsymbol{E})$; and $\overline{\boldsymbol{\sigma}}^P$ is the average contribution due to the presence of the particle. The stresslet $\boldsymbol{S}_B$ for the rigid slender body suspended between the bounding walls is given by (Batchelor 1971)

$$\boldsymbol{S}_B = -\int_{-L/2}^{L/2} \left[\boldsymbol{F}_B(s_B)\boldsymbol{p}_B - \frac{1}{3}\boldsymbol{I}\{\boldsymbol{F}_B(s_B) \cdot \boldsymbol{p}_B\} \right] s_B \, \mathrm{d}s_B \tag{5.2}$$

for an instantaneous configuration. Using the linearized expression for the line force density $\boldsymbol{F}_B(s_B)$ on the bulk fibre (2.6) and integrating along the axis gives

$$\boldsymbol{S}_B = -(\boldsymbol{\mathscr{T}}_B \times \boldsymbol{p}_B)\boldsymbol{p}_B - S_B\left(\boldsymbol{p}_B\boldsymbol{p}_B - \frac{1}{3}\boldsymbol{I}\right). \tag{5.3}$$

Note that we ignore the direct contribution of repulsive forces between the wall and bulk particle when calculating the stress. Consequently, the torque $\boldsymbol{\mathscr{T}}_B$ in (5.3) contains contributions only from Brownian motion. The relation between the stresslet coefficient S_B and the particle stress is also made clear in (5.3).

Calculating the effective stress contribution of the rigid fibre requires averaging (5.3) over the orientation and centre-of-mass distributions. This average is calculated from the simulations by sampling the distributions at steady state (§ 5.1) and then from theory at the same level of approximation as used in § 3.1 for predicting the centre-of-mass distribution (§ 5.2). Results are presented comparing the calculated value of the total contribution, as well as individual contributions (§ 5.3).

5.1. *Calculation of extra particle stress from simulations*

Once the distribution has approached steady state ($t > Pe\dot{\gamma}^{-1}$), the instantaneous value of the particle stresslet from (5.2) is sampled N_R times from the simulation results and averaged,

$$\overline{\boldsymbol{\sigma}}^P = \frac{n_d}{N_R} \sum_{l=1}^{N_R} [\boldsymbol{S}_B]_l, \tag{5.4}$$

to give the mean expected value for the extra particle stress. Here n_d is the number density N/V. The number of rods in each periodic cell is $N = 1$, and the volume V represents the space between the bounding walls at which the bulk particle resides, rather than the entire volume of the periodic cell. Calculating this volume while accounting for the bumpy walls gives

$$V = b_x b_z H - \frac{\pi L^3}{4A^2} \frac{N_W}{2}, \tag{5.5}$$

where N_W is the total number of wall particles. The number density is consequently $N/V = 1.876 \times 10^{-2} L^{-3}$ in all of these simulations.

Note that the shear stress for the confined flow can be calculated from the simulation results in two ways: as above from the particle stresslets or by normalizing the total force acting on the walls in the x-direction by the area. The forces on the wall due to the fluid in the absence of a particle must be subtracted from the total values in order to isolate the contribution from the particles. The expected value of the fluid stress matches within 1.38 % of the result from simulations in the absence of particles and the mean value of the particle contribution to the shear stress as calculated from the stresslets, and the wall forces agrees within at least 0.04 % for all cases.

Figure 16(*a*) shows the total contribution of the particle stress for values of Pe between 1.2×10^3 and 1.2×10^5; the values of $\overline{\sigma}_{xy}^P$ have been normalized by $n_d L^3 \mu \dot{\gamma}$. Even at the lowest Pe of 1.2×10^3, for which the particle stress is largest, the normalized $\overline{\sigma}_{xy}^P$ is only 8.58×10^{-3}, demonstrating the relatively small impact of the dilute suspension of rods on the overall rheology. The extra particle shear stress $\overline{\sigma}_{xy}^P$ can be separated into components,

$$\overline{\sigma}_{xy}^P = \overline{\sigma}_{xy}^{PB} + \overline{\sigma}_{xy}^{PS}, \tag{5.6}$$

arising from the Brownian torque $\overline{\sigma}_{xy}^{PB}$ and the shear flow $\overline{\sigma}_{xy}^{PS}$. Each is generated independently from (5.3),

$$\overline{\sigma}_{xy}^{PB} = \frac{n_d}{N_R} \sum_{l=1}^{N_R} [-p_y(\mathcal{T}_B \times \boldsymbol{p}_B) \cdot \hat{\boldsymbol{x}}]_l \tag{5.7}$$

and

$$\overline{\sigma}_{xy}^{PS} = \frac{n_d}{N_R} \sum_{l=1}^{N_R} [-S_B p_x p_y]_l, \tag{5.8}$$

and then averaged as described in (5.4). The result for each contribution is shown in figures 16(*b*) and 16(*c*). Not surprisingly since Pe is large, the contribution from shear exceeds that from the Brownian rotation by orders of magnitude.

5.2. *Prediction of extra particle stress using theory*

To compare the stress calculation from the simulation as described in the previous section with the theoretical calculation, the approach of the previous theory
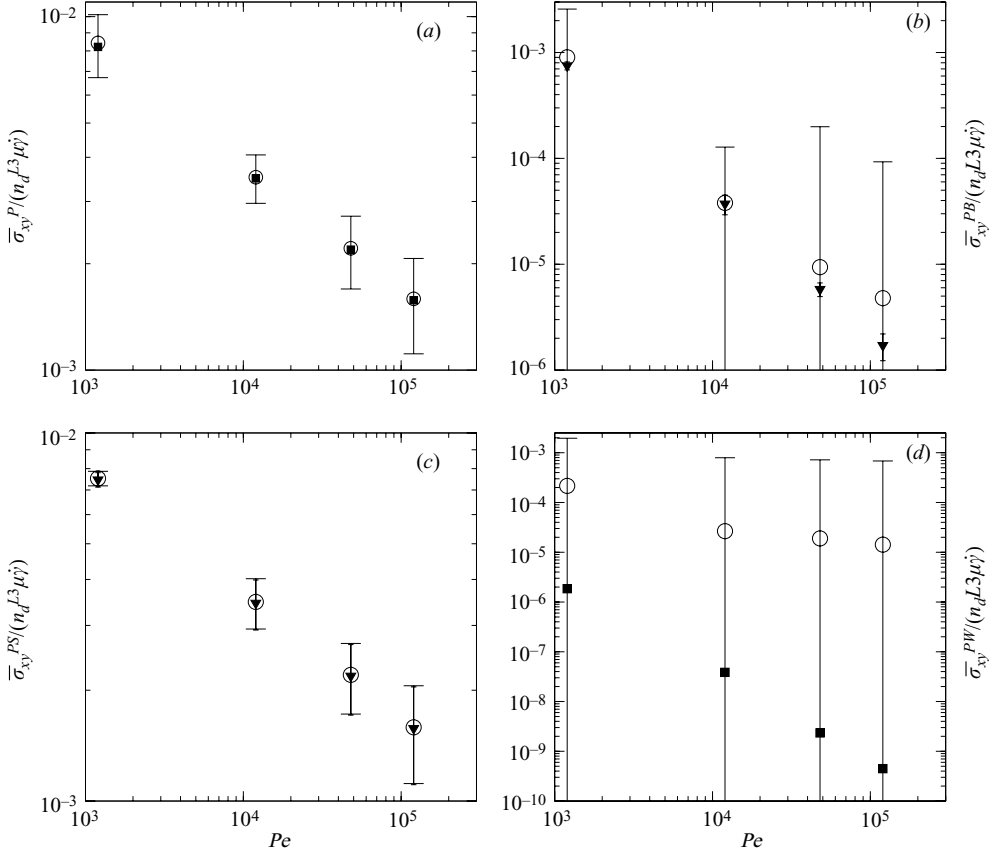
FIGURE 16. The extra particle shear stresses for rigid fibres with $A = 10$ under simple shear flow between two walls with a gap of $H = 6L$ calculated from simulation (○), simulated orientation moments (▼) and theory (■). Results shown include (*a*) the total particle stress $\overline{\sigma}_{xy}^{P}$, (*b*) the Brownian torque contribution $\overline{\sigma}_{xy}^{PB}$, (*c*) the shear flow contribution $\overline{\sigma}_{xy}^{PS}$ and (*d*) the additional contributions due to presence of the wall $\overline{\sigma}_{xy}^{PW}$.

(Park *et al.* 2007) which uses the approximate linearized Green's function is applied directly to calculate the stress using (5.3). For the Brownian torque, the expression as given in (3.6) is used. The explicit result for the stresslet coefficient is given by

$$S_B = -\frac{\pi\mu L^3 \dot{\gamma}}{6\ln(2A)} p_x p_y - \lambda(r_y) \left[2p_y \boldsymbol{p}_B + \left(p_y^2 - 1 \right) \hat{\boldsymbol{y}} \right] \cdot \mathscr{F}_B, \qquad (5.9)$$

where the first term is the direct contribution of the shear flow. Upon substitution of (3.6) for the Brownian force,

$$S_B = -\frac{\pi\mu L^3 \dot{\gamma}}{6\ln(2A)} p_x p_y + k_B T \lambda(r_y) \left[2p_y \boldsymbol{p}_B + \left(p_y^2 - 1 \right) \hat{\boldsymbol{y}} \right] \cdot \frac{\partial \ln \Psi}{\partial \boldsymbol{r}_B}, \qquad (5.10)$$

it becomes clear that the second term is related to the gradient in the centre-of-mass distribution which is created by the hydrodynamic interaction of the rod and bounding walls.

Replacing $\mathscr{T}_B$ and S_B in (5.3) with (3.6) and (5.10) gives an expression for the stresslet,

$$\boldsymbol{S}_B = k_B T \boldsymbol{p}_B \left(\boldsymbol{I} - \boldsymbol{p}_B \boldsymbol{p}_B \right) \cdot \frac{\partial \ln \Psi}{\partial \boldsymbol{p}_B} + \frac{\pi \mu L^3 \dot{\gamma}}{6 \ln(2A)} p_x p_y \left(\boldsymbol{p}_B \boldsymbol{p}_B - \frac{1}{3} \boldsymbol{I} \right)$$

$$- k_B T \lambda(r_y) \left(\boldsymbol{p}_B \boldsymbol{p}_B - \frac{1}{3} \boldsymbol{I} \right) \left[2 p_y \boldsymbol{p}_B + \left(p_y^2 - 1 \right) \hat{\boldsymbol{y}} \right] \cdot \frac{\partial \ln \Psi}{\partial \boldsymbol{r}_B}, \quad (5.11)$$

which must be averaged to give the mean stress. The average is performed over the expected configuration in the system of volume V,

$$\overline{\boldsymbol{\sigma}}^P = n_d \iint \Psi \boldsymbol{S}_B \, \mathrm{d}\boldsymbol{p}_B \, \mathrm{d}\boldsymbol{r}_B. \quad (5.12)$$

By factorizing the distribution function $\Psi = n\psi$ under the same assumption that orientation distribution is not influenced by the wall and equilibrates faster than n, this equation is completed in terms of the ensemble average over the orientation distribution ψ,

$$\frac{\overline{\boldsymbol{\sigma}}^P}{n_d L^3 \mu \dot{\gamma}} = \frac{4\pi}{Pe \ln(2A)} (3\langle \boldsymbol{p}_B \boldsymbol{p}_B \rangle - \boldsymbol{I}) + \frac{\pi}{6 \ln(2A)} \left(\langle p_x p_y \boldsymbol{p}_B \boldsymbol{p}_B \rangle - \frac{1}{3} \boldsymbol{I} \langle p_x p_y \rangle \right)$$

$$+ \frac{4\pi}{Pe \ln(2A)} \int n\lambda(r_y) \frac{\partial \ln n}{\partial r_y} \, \mathrm{d}r_y \left[\langle \boldsymbol{p}_B \boldsymbol{p}_B \rangle + \boldsymbol{I} \left(\langle p_y^2 \rangle - \frac{1}{3} \right) - 3 \langle p_y^2 \boldsymbol{p}_B \boldsymbol{p}_B \rangle \right] \quad (5.13)$$

The first two contributions correspond to those of a dilute system of Brownian fibres in an unbounded flow as derived by Hinch & Leal (1976). The first represents the affect of the Brownian torque on the effective stress, which vanishes at high Pe in comparison to the second term representing the effect of the shear flow. The third term in (5.13) is a contribution to the effective stress from the non-uniform distribution of the centre of mass of the rods caused by the migration.

The shear stress component (xy) of $\overline{\boldsymbol{\sigma}}^P$ can be evaluated as a function of Pe from (5.13), using the analytical expression obtained in §3 for $n(r_y)$ and numerically integrating $\lambda(r_y)\partial n/\partial r_y$ over the channel height. The results are plotted in figure 16(a). The additional contribution from the inhomogeneous distribution is labelled $\overline{\sigma}_{xy}^{PW}$ (the third term in (5.13)) and is small as seen in figure 16(d).

5.3. *Comparison of stress calculations*

Figure 16(a) shows that the effective particle stress as calculated from the simulation results, and the theoretical description closely agree. The close agreement, given the small contribution from the inhomogeneous distribution in the theory, implies that the effective particle stress is close to that of a dilute suspension of Brownian fibres in the absence of bounding walls.

To investigate the effects of the bounding walls, as well as periodic images, on the results calculated from the simulations, we calculate the dilute contribution evaluated directly from the simulations. The contribution from the Brownian torque, given by

$$\frac{\overline{\sigma}_{xy}^{PB}}{n_d L^3 \mu \dot{\gamma}} = \frac{12\pi}{Pe \ln(2A)} \langle p_x p_y \rangle, \quad (5.14)$$

is calculated using the moment of $p_x p_y$ as sampled from the simulations and averaged over the channel height. The result, plotted in figure 16(b), shows that the dilute contribution is slightly lower than the value calculated directly from the simulation.

Likewise, figure 16(c) shows the contribution from the shear for which the value

$$\frac{\overline{\sigma}_{xy}^{PS}}{n_d L^3 \mu \dot{\gamma}} = \frac{\pi}{6\ln(2A)} \langle p_x{}^2 p_y^2 \rangle \tag{5.15}$$

was calculated from the orientation moments extracted from the simulation. The result is only slightly lower than the prediction made directly from the simulation results as given by (5.8).

The difference in the total particle stress from the simulations as given by (5.6) and the dilute value as calculated from the orientation moments produced by the simulations by combining (5.14) and (5.15) is given in figure 16(d). This quantity represents the additional stress due to the walls, inhomogeneous distribution for the centre of mass and interactions with the periodic images. Figure 16(d) shows that the value predicted from the theory for the contribution beyond that of a dilute suspension in the absence of walls is much smaller than that predicted by the simulations.

The lack of agreement shown in figure 16(d) clearly arises from the approximations made within the theory for the Green's functions. The theory predicts an additional contribution to the stress from the presence of the inhomogeneous distribution but does not fully account for the reduction in the stresslet coefficient due to direct interactions with the bounding walls and other mechanisms. Improved approximations for the evaluation of the Green's function could improve the agreement with the simulation results.

That the presence of walls can affect the rheology of suspension systems is a well-known result (Happel & Brenner 1965). For the specific case of Brownian rods, Schiek & Shaqfeh (1995) calculated the stress for a bound suspension at low values of *Pe* using a non-local theory and accounting for the excluded volume but not hydrodynamic interactions which alter the probability distribution. The increasing confinement of the rods reduced the effective viscosity further as compared to an unbounded suspension. The analysis presented in (5.1)–(5.3) is based upon a local approximation but does account for the dependence of the stress upon the position of the rod. For the conditions studied here, the difference between the bounded and unbounded results is about 2 % at best. A direct investigation of the dependence of the stress upon particle position is given in figure 17, which shows the instantaneous value of the effective particle stress as calculated from the simulations normalized by the dilute value for two different orientations. The particle stress is only about 1 % higher than the unbounded value at $r_y = 0.5L$ and vanishes to less than 0.3 % of the value at the centre. Only a small amount of additional stress is found to exist even for particles very near a wall; consequently the fact that the average particle stress closely matches the dilute values is not surprising at high *Pe* at which the particle migrates away from the bounding walls. The limited effect of the walls on the rheology of dilute suspensions of rods has been noted by others (Attansio *et al.* 1972; Ganani & Powell 1985; Petrie 1999; Moses, Advani & Reinhardt 2001; Zurita-Gotor, Bławzdziewicz & Wajnryb 2007).

6. Conclusions

Detailed comparisons with simulations demonstrate that an extended version of the kinetic theory of Park *et al.* (2007) can adequately predict the centre-of-mass distribution for a rigid fibre suspended between two plane walls in either simple shear or parabolic flow of sufficiently high strength or *Pe*. For these large *Pe*, the good agreement validates that the multiple approximations made in the theory do not have
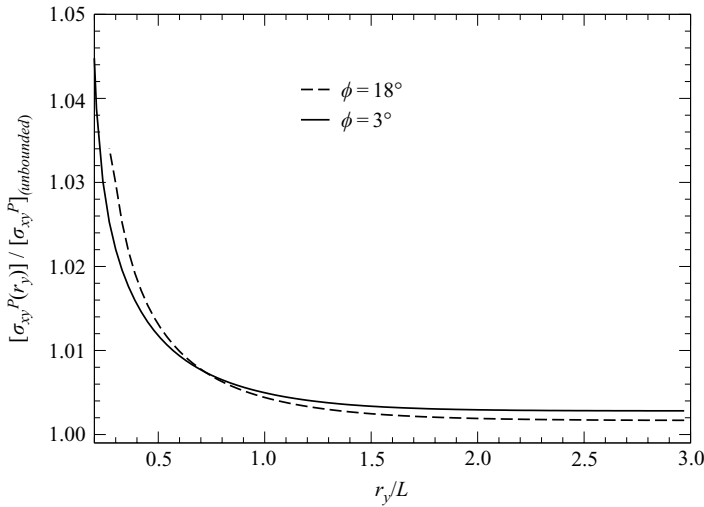
FIGURE 17. The particle shear stresses $\sigma_{xy}^P(r_y)$ for a rigid fibre with $\phi = 3°$, $18°$, $p_z = 0$ and $A = 10$ in a gap of $H = 6L$, normalized by the theoretical values with the same configurations in unbounded flow, as functions of a distance from a wall, r_y/L. Calculations are from the simulation with simple shear flow with a force and torque-free fibre.

a severe adverse affect upon the predictions for the conditions studied. The success of the theory at high rates of shear is due to the hydrodynamic interaction lifting the particles a significant distance from the wall, where the lack of quantitative differences in the instantaneous prediction of the lift velocity are small (§4), and the particle orientation distribution conforms to that of an unbounded flow (figures 13 and 15).

The theory cannot be applied with confidence if $Pe \leqslant 1.2 \times 10^3$ for the case studied here of $A = 10$ and $H = 6L$. The steric interactions between the rod and bounding walls, which are ignored in the current version of the kinetic theory, control the thickness and shape of the depletion layer at these lower rates of shear at which the hydrodynamic lift force is too weak to move the particle out of range of the wall. A theory capable of making accurate predictions over a wider range Pe should include the steric interactions as done in previous investigations (de Pablo *et al.* 1992; Hijazi & Khater 2001).

Simulations presented in the current work were limited to the conditions of $A = 10$ and $H = 6L$. The theory, which relies on a superposition of the Green's function for plane walls, will become continually less accurate as the gap width H becomes smaller with regard to the particle length L. Simulations of the migration of flexible polymers (Usta *et al.* 2007) indicate that theoretical predictions for the rigid rod distribution would be greatly in error for $H \lesssim 5L$. Conversely, the theory is expected to become more accurate as the ratio H/L increases, and comparisons with simulations of Saintillan *et al.* (2006*a*) on parabolic flow suggest that the hydrodynamic lift force remains of importance at lower Pe within larger channels, again conforming to expectations.

The bounding walls alter the particle contribution to the total stress little as compared to the dilute values in an unbounded system owing to the strong migration away from the bounding walls at high Pe. Differences between evaluations of the particle stress from the simulations and a theoretical calculation at the same level of

approximation used to predict the distribution are attributable to the approximate evaluation of the Green's function and can likely be improved upon.

This simulation method will be extended to study the rheology and structure with semi-dilute and concentrated systems of rods at high *Pe*. Previous simulations, such as those of Sundararajakumar & Koch (1997) and Pryamitsyn & Ganesan (2008), examined the rheology of unbounded shear flow. The net migration caused by hydrodynamic interaction with the walls in a non-dilute system would be expected to alter the microstructure, which is directly related to the rheological properties (Shaqfeh & Fredrickson 1990; Dhont & Briels 2003). The results may be useful in explaining the shear thinning behaviour observed for semi-dilute suspensions of fibres at high *Pe* (Ganani & Powell 1985; Chaouche & Koch 2001; Bricker, Park & Butler 2008).

REFERENCES

AGARWAL, U. S., DUTTA, A. & MASHELKAR, R. A. 1994 Migration of macromolecules under flow: the physical origin and engineering implications. *Chem. Engng Sci.* **49**, 1693–1717.

ASOKAN, K., RAMAMOHAN, T. R. & KUMARAN, V. 2002 A novel approach to computing the orientation moments of spheroids in simple shear flow at arbitrary Péclet number. *Phys. Fluids* **14**, 75–84.

ATTANSIO, A., BERNINI, U., GALLOPO, P. & SEGRE, G. 1972 Significance of viscosity measurements in macroscopic suspensions of elongated particles. *Trans. Soc. Rheol.* **16**, 147–154.

AUSSERRE, D., EDWARDS, J., LECOURTIER, J., HERVET, H. & RONDELEX, F. 1991 Hydro-dynamic thickening of depletion layers in colloidal solutions. *Europhys. Lett.* **14**, 33–38.

BATCHELOR, G. K. 1970 Slender-body theory for particles of arbitrary cross-section in Stokes flow. *J. Fluid Mech.* **44**, 419–440.

BATCHELOR, G. K. 1971 The stress generated in a non-dilute suspension of elongated particles by pure straining motion. *J. Fluid Mech.* **46**, 813–829.

BEENAKKER, C. W. J. 1986 Ewald sum of the Rotne–Prager tensor. *J. Chem. Phys.* **85**, 1581–1582.

BLAKE, J. R. 1971 A note on the image system for a Stokeslet in a no-slip boundary. *Proc. Cambridge Phil. Soc.* **70**, 303–310.

BRENNER, H. 1974 Rheology of a dilute suspension of axisymmetric Brownian particles. *Intl J. Multiphase Flow* **1**, 195–341.

BRICKER, J. M. & BUTLER, J. E. 2007 Correlation between structures and microstructures in concentrated suspensions of non-Brownian spherical particles subject to unsteady shear flows. *J. Rheol.* **51**, 735–759.

BRICKER, J. M., PARK, H.-O. & BUTLER, J. E. 2008 Rheology of semidilute suspensions of rigid polystyrene ellipsoids at high Péclet numbers. *J. Rheol.* **52**, 941–955.

BUTLER, J. E. & SHAQFEH, E. S. G. 2002 Dynamic simulations of the inhomogeneous sedimentation of rigid fibers. *J. Fluid Mech.* **468**, 205–237.

BUTLER, J. E. & SHAQFEH, E. S. G. 2005 Brownian dynamics simulations of a flexible polymer chain which includes continuous resistance and multibody hydrodynamic interactions. *J. Chem. Phys.* **122**, 01491.

BUTLER, J. E., USTA, O. B., KEKRE, R. & LADD, A. J. C. 2007 Kinetic theory of a confined polymer driven by an external force and pressure-driven flow. *Phys. Fluids* **19**, 113101.

CHAOUCHE, M. & KOCH, D. L. 2001 Rheology of non-Brownian rigid fiber suspensions with adhesive contacts. *J. Rheol.* **45**, 369–382.

CHEN, S. B. & JIANG, L. 1999 Orientation distribution in a dilute suspension of fibers subject to simple shear flow. *Phys. Fluids* **11**, 2878–2890.

CHEN, S. B. & KOCH, D. L. 1996 Rheology of dilute suspensions of charged fibers. *Phys. Fluids* **8**, 2792–2807.

CLAEYS, I. L. & BRADY, J. F. 1989 Lubrication singularites of the grand resistance tensor for two arbitrary particles. *Physico-Chem. Hydrodyn.* **11**, 261–293.

Cobb, P. D. & Butler, J. E. 2005 Simulations of concentrated suspensions of rigid fibers: relationship between short-time diffusivities and the long-time rotational diffusion. *J. Chem. Phys.* **123**, 054908.

Cox, R. G. 1970 The motion of long slender bodies in a viscous fluid. Part 1. General theory. *J. Fluid Mech.* **44**, 791–810.

Dhont, J. K. G. & Briels, W. J. 2003 Inhomogeneous suspensions of rigid rods in flow. *J. Chem. Phys.* **118**, 1466.

Doi, M. & Edwards, S. F. 1986 *The Theory of Polymer Dynamics*. Oxford University Press.

Fang, L., Hu, H. & Larson, R. 2005 DNA configuration and concentration in shearing flow near a glass surface in a microchannel. *J. Rheol.* **49**, 127.

Fixman, M. 1978 Simulation of polymer dynamics. Part 1. General theory. *J. Chem. Phys.* **69**, 1527–1537.

Ganani, E. & Powell, R. L. 1985 Suspensions of rodlike particles: literature review and data correlations. *J. Composite Mater.* **19**, 194–215.

Grassia, P. S., Hinch, E. J. & Nitsche, L. C. 1995 Computer simulations of Brownian motion of complex systems. *J. Fluid Mech.* **282**, 373–403.

Happel, J. & Brenner, H. 1965 *Low Reynolds Number Hydrodynamics*. Prentice Hall.

Harlen, O. G., Sundararajakumar, R. R. & Koch, D. L. 1999 Numerical simulation of a sphere settling through a suspension of neutrally buoyant fibers. *J. Fluid Mech.* **388**, 355–388.

Hasimoto, H. 1959 On the periodic fundamental solutions of the Stokes equations and their application to viscous flow past a cubic array of spheres. *J. Fluid Mech.* **5**, 317–328.

Hernández-Ortiz, J. P., de Pablo, J. J. & Graham, M. D. 2006 Cross-stream-line migration in confined flowing polymer solutions: theory and simulation. *Phys. Fluids* **18**, 123101.

Hijazi, A. & Khater, A. 2001 Brownian dynamics simulations of rigid rod-like macromolecular particles flowing in bounded channels. *Comput. Mater. Sci.* **22**, 279–290.

Hijazi, A. & Zoaeter, M. 2002 Brownian dynamics simulations of rigid rod-like particles in dilute flowing solution. *Eur. Polym. J.* **38**, 2207–2211.

Hinch, E. J. & Leal, L. G. 1972 The effect of Brownian motion on the rheological properties of suspension of non-spherical particles. *J. Fluid Mech.* **52**, 683–712.

Hinch, E. J. & Leal, L. G. 1976 Constitutive equations in suspension mechanics. Part 2. Approximate forms for a suspension of rigid particles affected by Brownian rotations. *J. Fluid Mech.* **76**, 187–208.

Hoda, N. & Kumar, S. 2007a Brownian dynamics simulations of polyelectrolyte adsorption in shear flow with hydrodynamic. *J. Chem. Phys.* **127**, 234902.

Hoda, N. & Kumar, S. 2007b Kinetic theory of polyelectrolyte adsorption in shear flow. *J. Rheol.* **51**, 799–820.

Hoda, N. & Kumar, S. 2008 Brownian dynamics simulations of polyelectrolyte adsorption in shear flow: effects of solvent quality and charge patterning. *J. Chem. Phys.* **128**, 164907.

Holm, R. & Söderberg, D. 2007 Shear influence on fibre orientation: dilute suspension in the near wall region. *Rheol. Acta* **46**, 721–729.

Hsu, R. & Ganatos, P. 1976 Gravitational and zero-drag motion of a spheroid adjacent to an inclined plane at low Reynolds number. *J. Fluid Mech.* **268**, 267.

Jendrejack, R. M., Schwartz, D. C., de Pablo, J. J. & Graham, M. D. 2004 Shear-induced migration in flowing polymer solutions: simulation of long-chain DNA in microchannels. *J. Chem. Phys.* **120**, 2513–2519.

Leal, L. G. & Hinch, E. J. 1971 The effect of weak Brownian rotation on particles in shear flow. *J. Fluid Mech.* **46**, 685–703.

Liron, N. & Mochon, S. 1976 Stokes flow for a Stokeslet between two parallel flat plates. *J. Engng Math.* **10**, 287–303.

Ma, H. & Graham, M. 2005 Theory of shear-induced migration in dilute polymer solutions near solid boundaries. *Phys. Fluids* **17**, 083103.

Mody, N. A. & King, M. R. 2005 Three-dimensional simulations of a platelet-shaped spheroid near a wall in shear flow. *Phys. Fluids* **17**, 113302.

Morse, D. C. 2004 Theory of constrained Brownian motion. *Adv. Chem. Phys.* **128**, 65–189.

Moses, K. B., Advani, S. G. & Reinhardt, A. 2001 Investigation of fiber motion near solid boundaries in simple shear flow. *Rheol. Acta* **40**, 296–306.

NITSCHE, L. C. & HINCH, E. J. 1997 Shear-induced lateral migration of Brownian rigid rods in parabolic channel flow. *J. Fluid Mech.* **332**, 1–21.

NITSCHE, J. M. & ROY, P. 1996 Shear-induced alignment of nonspherical Brownian particles near walls. *AIChE J.* **42**, 2729–2742.

NOTT, P. R. & BRADY, J. F. 1994 Pressure-driven flow of suspensions: simulation and theory. *J. Fluid Mech.* **275**, 157–199.

OLLA, P. 1999 Simplified model for red cell dynamics in small blood vessels. *Phys. Rev. Lett.* **82**, 453–456.

DE PABLO, J. J., OTTINGER, H. C. & RABIN, Y. 1992 Hydrodynamic changes of the depletion layer of dilute polymer solutions near a wall. *AIChE J.* **38**, 273–283.

PARK, J., BRICKER, J. M. & BUTLER, J. E. 2007 Cross-stream migration in dilute solutions of rigid polymers undergoing rectilinear flow near a wall. *Phys. Rev. E* **76**, 040801.

PETRIE, C. J. S. 1999 The rheology of fibre suspensions. *J. Non-Newton. Fluid Mech.* **87**, 369–402.

PRYAMITSYN, V. & GANESAN, V. 2008 Screening of hydrodynamic interactions in Brownian rod suspensions. *J. Chem. Phys.* **128**, 134901.

ROTNE, J. & PRAGER, S. 1969 Variational treatment of hydrodynamic interaction in polymers. *J. Chem. Phys.* **50**, 4831–4837.

SAINTILLAN, D., SHAQFEH, E. S. G. & DARVE, E. 2006a Effect of flexibility on the shear-induced migration of short-chain polymers in parabolic channel flow. *J. Fluid Mech.* **557**, 297–306.

SAINTILLAN, D., SHAQFEH, E. S. G. & DARVE, E. 2006b The growth of concentration fluctuations in dilute dispersions of orientable and deformable particles under sedimentation. *J. Fluid Mech.* **553**, 347–388.

SAINTILLAN, D., SHAQFEH, E. S. G. & DARVE, E. 2006c Hydrodynamic interactions in the induced-charge electrophoresis of colloidal rod dispersions. *J. Fluid Mech.* **563**, 223–259.

SCHIEK, R. L. & SHAQFEH, E. S. G. 1995 A nonlocal theory for stress in bound, Brownian suspensions of slender, rigid fibers. *J. Fluid Mech.* **296**, 271–324.

SCHIEK, R. L. & SHAQFEH, E. S. G. 1997 Cross–streamline migration of slender Brownian fibres in plane Poiseuille flow. *J. Fluid Mech.* **332**, 23–39.

SHAQFEH, E. S. G. & FREDRICKSON, H. 1990 The hydrodynamic stress in a suspension of rods. *Phys. Fluids* A **2**, 7–24.

SINGH, A. & NOTT, P. 2000 Normal stresses and microstructure in bounded sheared suspensions via Stokesian dynamics simulations. *J. Fluid Mech.* **412**, 279–301.

STABEN, M. E., ZINCHENKO, A. Z. & DAVIS, R. H. 2003 Motion of a particle between two parallel plane walls in low-Reynolds-number Poiseuille flow. *Phys. Fluids* **15**, 1711–1733.

STONE, H. A., STROOCK, A. D. & AJDARI, A. 2004 Engineering flows in small devices: microfluidics towards a lab-on-a-chip. *Annu. Rev. Fluid Mech.* **36**, 381–411.

STOVER, C. A. & COHEN, C. 1990 The motion of rodlike particles in the pressure-driven flow between two flat plates. *Rheol. Acta* **29**, 192–203.

STOVER, C. A., KOCH, D. L. & COHEN, C. 1992 Observations of fibre orientation in simple shear flow of semi-dilute suspensions. *J. Fluid Mech.* **238**, 277–296.

SUNDARARAJAKUMAR, R. R. & KOCH, D. L. 1997 Structure and properties of sheared fiber suspensions with mechanical contacts. *J. Non-Newton. Fluid Mech.* **73**, 205–239.

TORNBERG, A.-K. & GUSTAVSSON, K. 2006 A numerical method for simulations of rigid fiber suspensions. *J. Comput. Phys.* **215**, 172–196.

USTA, O. B., BUTLER, J. E. & LADD, A. J. C. 2006 Flow induced migration of polymers in dilute solution. *Phys. Fluids* **18**, 031703.

USTA, O. B., BUTLER, J. E. & LADD, A. J. C. 2007 Transverse migration of a confined polymer driven by an external force. *Phys. Rev. Lett.* **98**, 098301.

YANG, S. M. & LEAL, L. G. 1984 Particle motion in Stokes flow near a plane fluid-fluid interface. Part 2. Linear shear and axisymmetric straining flows. *J. Fluid Mech.* **149**, 275–304.

ZURITA-GOTOR, M., BŁAWZDZIEWICZ, J. & WAJNRYB, E. 2007 Motion of a rod-like particle between parallel walls with application to suspension rheology. *J. Rheol.* **51**, 71–97.